THESIS FOR THE DEGREE OF LICENTIATE OF ENGINEERING

Interphases at Interfaces in Solid-State Batteries

ELIN DUFVENIUS ESPING

Department of Physics & Astronomy
CHALMERS UNIVERSITY OF TECHNOLOGY
Gothenburg, Sweden, 2026

Interphases at Interfaces in Solid-State Batteries

Elin Dufvenius Esping

Department of Physics & Astronomy
Chalmers University of Technology
SE-412 96 Göteborg,
Sweden
Phone: +46(0)31 772 1000

Cover:
Interphase formation inside the lithium metal electrode
and its internal structure consisting of multiple difference phases.

Printed by Chalmers Digitaltryck,
Gothenburg, Sweden 2026.

Interphases at Interfaces in Solid-State Batteries

ELIN DUFVENIUS ESPING

Department of Physics & Astronomy
Chalmers University of Technology

Abstract

Lithium-metal solid-state batteries offer compelling energy density and safety advantages over conventional lithium-ion batteries, but their practical implementation is limited by interfacial instability. The interface between the lithium metal anode and sulphide-based solid-state electrolytes (e.g. $\mathrm{Li_6PS_5Cl}$) is thermodynamically unstable, and the interphase that forms through chemical and electrochemical degradation governs the long-term cycling performance. In this work, we investigate interphase formation and reversibility at the $\mathrm{Li/Li_6PS_5Cl}$ interface, combining electrochemical characterization with multimodal X-ray characterization. Coulometric titration time analysis is used to quantify interfacial side reaction kinetics and resolve the electrochemical signatures of individual stages of interphase formation, including the role of phosphorus species and their lithiation state. To directly correlate electrochemical signatures with structural and chemical changes, micro- and nano-X-ray computed tomography were combined with X-ray diffraction computed tomography. This revealed that degradation products do not form homogeneously at the interface, but instead accumulate locally. At the nanoscale, this locally formed interphase is composed of distinctly different phases. The results demonstrate that chemically and electrochemically induced degradation produce distinct chemical and morphological differences at the interface. These findings provide new mechanistic insight into interphase growth at the lithium metal/sulphide solid-state electrolyte interface.

Keywords

solid-state-battery, lithium metal, interphase formation, X-ray imaging

Appended publications

This thesis is based on the following publications:

I **E . D. Esping**, S. Lindberg, A. Matic,
Electrochemical Signatures of Interphase Formation in Lithium-metal Solid-State Batteries
In Manuscript.

II **E. D. Esping**, A. Erlandsson, J. Rizell, M. Afiandika, T. E. K. Christensen, G. P. Forero, I. Kantor, V. Vanpeene, A. Matic,
Revealing Multiphase Formation at the Lithium-metal Solid-State Electrolyte Interface
In Manuscript.

Contribution Report

I. EDE planned and carried out the experiments with input from AM. EDE performed all data analyses, wrote the first draft of the manuscript. SL, and AM participated in the discussion of results, and revision of the manuscript.

II. EDE planned and carried out the experiments with input from JR, VV and AM. AE, JR, MA, TEKC, GPF, IK, VV, and AM helped carry out the synchrotron experiments. EDE performed all data analyses with JR and VV participating in discussion and preparation. EDE wrote the first draft of the manuscript with AM participating in discussion and planning of the manuscript and of results. EDE revised it with all co-authors.

Publications not Included in this Thesis

I Q. Wu, **E. D. Esping**, M. Afiandika, S. Xiong, A. Matic,
Understanding the electro-chemo-mechanics of lithium metal anodes
eScience, 6, 1, (2026), 100429.

Acknowledgements

Just like no synchrotron experiment survives without its beam-team, this work is the result of collaboration, support, and encouragement from many people, all of whom deserve my deepest thanks.

Solid-state electrolytes conduct best under pressure. So, it turns out, do I. But thank you to my supervisor, Aleksandar Matic, for not letting me crack under pressure (unlike some solid electrolytes...). Thank you for your guidance, encouragement, and for giving me the freedom to dive in head-first and carve out my own path through the solid-state world. Thank you for opening the door to the wonders of X-rays, rescuing me from the dark, dark magic that is impedance spectroscopy, and making this experience deeply challenging and immensely rewarding.

To my co-supervisor, Victor Vanpeene, thank you for stepping into my project midway with such grace and energy. You are a true tomography wizard and an endless source of knowledge. You continually inspire me by showing me new ways to analyse data and, perhaps more importantly, by always managing to see the good even in my cracked samples.

I also want to extend my thanks to my examiner Lars Börjesson, and to Ezio Zanghellini who somehow has a solution to every problem. To everyone in Professor Hwang's group in Korea, thank you for welcoming me so warmly and making my stay in South Korea such a memorable chapter of this journey. I sincerely hope you will allow me to return.

To my colleagues at MF, both past and present, what we have is something truly special, and I am endlessly grateful for the joy, camaraderie, and support you have brought into this experience, and to all colleagues turned friends. In this group of people I met the first tomography wizards, Martina and Josef. You have both been such an inspiration and guiding hand for a young researcher. To Andreas, my former Master's thesis student, thank you for not only deciding to stay and become an excellent PhD student, but also for continuing to work with solid-state batteries despite my supervision. A huge part of my wonderful time here comes from my lovely office colleagues. To Marita, the ever-shining ray of sunshine, to the kind-hearted Quan, indisputably the most stylish among us, and to Sofia, who deserves an acknowledgement section longer than the actual science in this thesis, keep on twinning!

This work would never have been possible without the incredible beamline scientists I have had the privilege to meet, at MAX IV and at ESRF, and everyone within the BatteryHub. I am also grateful to the Swedish Energy Agency for funding and supporting this work.

Finally, to my friends and family, thank you for your unwavering support, for grounding me when things became overwhelming, and for celebrating every step along the way. You have been the constant in a process full of variables, and I would not have made it here without you.

Table of Contents

Chapter 1

Introduction

Electrochemistry is, in many respects, an interfacial science. When an electrode comes into contact with an electrolyte, an interface is formed. This boundary is central for electrochemical reactions [1]. When an electrode operates outside the thermodynamic stability window of the electrolyte, an interphase can form, a chemically and structurally distinct layer formed through decomposition reactions [1]. This thesis focuses on these two closely linked concepts, interfaces and interphases.

Nowhere is the importance of such interfaces more evident than in batteries. Since their commercialisation in the 1990s, lithium-ion batteries have transformed energy storage, enabling portable electronics and electric vehicles [2–4]. At the core of their operation lies the electrode/electrolyte interface, where lithium-ions and electrons are exchanged in reduction-oxidation reactions during charge and discharge [5]. To achieve high energy densities, electrodes are driven to extreme potentials, often beyond the thermodynamic stability limits of the electrolyte. As a result, the electrolyte decomposes at the interface, forming a solid electrolyte interphase (SEI) [6]. In lithium-ion batteries, the formation of an SEI is essential, as it prevents continuous electrolyte decomposition while enabling reversible lithium-ion transport [7, 8]. At the same time, its structure, composition, and stability are difficult to control, making it one of the most critical and complex components of electrochemical systems. Understanding and controlling such interfacial phenomena is therefore central to the development of improved energy storage technologies.

Despite its essential role, the SEI is also a fundamental limitation [7]. Its formation consumes active material (lithium), reducing efficiency, and its mechanical and chemical instabilities lead to continuous evolution during cycling. These challenges become even more pronounced when moving beyond conventional graphite anodes as the demands placed on batteries continue to grow with each new application [9]. Applications such as electric vehicles and grid storage impose increasing demands on energy storage, including higher energy density, long cycle life, broad temperature ranges, and improved safety [10, 11]. Together, these demands have raised the question of whether new battery chemistries are required.

One of the most promising strategies for increasing energy density is the use of lithium metal as the negative electrode (anode) [9, 12, 13]. Lithium metal offers a significantly higher theoretical capacity and a lower electrochemical potential than graphite. However, its high reactivity intensifies interfacial instability and lithium deposition is often uneven, leading to the growth of dendritic structures

[14, 15]. In liquid electrolyte systems, this results in poor efficiency, limited lifetime, and serious safety concerns. Solid-state electrolytes offer a potential route to overcome these limitations [13, 16, 17]. By replacing flammable liquid electrolytes with a solid electrolyte, they promise improved safety and mechanical rigidity that could suppress non-uniform lithium growth. Advances in solid-state ionics [18] have led to the development of materials with ionic conductivities comparable to liquid electrolytes such as the sulphide solid-state electrolyte Li_6PS_5Cl (LPSC [19]), bringing the concept of solid-state batteries closer to realisation. However, the transition from liquid to solid electrolytes does not eliminate interfacial challenges, but transforms them. Unlike liquids, solid electrolytes do not wet electrode surfaces or easily accommodate volume changes, leading to poor physical contact and increased mechanical constraints [20, 21]. At the same time, many solid electrolytes, LPSC included, are thermodynamically unstable against lithium metal, resulting in interphase formation [22–24]. As a consequence, the interface between lithium metal and solid electrolytes becomes one of the central challenges in solid-state batteries. Rather than being a secondary effect, the formation and evolution of the interphase at the interface ultimately governs cell performance, stability, and lifetime.

A central theme of this thesis is the nature of the processes occurring at the lithium metal/LPSC interface. Capturing the processes requires approaches that probe the interface during operation. For this reason, this thesis employs *in situ* and *operando* techniques, combining electrochemical methods with X-ray characterisation to investigate the chemical, structural, and morphological evolution of the interphase at the interface.

The work presented in this thesis is based mainly on the appended papers. In **Paper I**, we investigate the formation and evolution of the interphase at the lithium metal/LPSC interface using electrochemical characterization. By applying coulometric titration time analysis combined with impedance spectroscopy we identify distinct electrochemical signatures associated with electrolyte decomposition, lithium consumption, and the lithiation and delithiation of phosphorus containing phases in the formed interphase. The results demonstrate that the interphase remains electrochemically active and that its transport properties also depend on the lithiation state of the phosphorus species present in the interphase. In **Paper II**, we directly probe the lithium metal/LPSC interface using *in situ* and *operando* X-ray characterization. By combining micro- and nano-scale X-ray computed tomography with X-ray diffraction computed tomography, we reveal that the interphase does not form as a uniform layer. Instead, it grows locally into the lithium metal and develops a heterogeneous, multiphase structure at the nanoscale. Together, these studies aim to move beyond merely describing interphases, towards understanding their dynamics and ultimately controlling them. Whether lithium metal and solid electrolytes can coexist stably is, ultimately, an interfacial question. The work that follows in this thesis is an attempt to understand, and begin to answer, that question.

Chapter 2

Solid-State Batteries

The story of modern energy storage is, in many ways, the story of lithium. Among the numerous types of electrochemical energy conversion and storage technologies, the lithium-ion battery stands out as one of the most impactful developments in the history of electrochemistry. Much of its appeal originates from the unique physicochemical properties of lithium itself. The combination of its small atomic weight, extremely low reduction potential, and monovalent charge gives lithium qualities that are nearly impossible for other elements to rival [25]. These properties made the lithium-ion battery the enabling technology of the wireless revolution and support the electrification of the transport sector [2].

Fundamental Principle of Rechargeable Batteries

At its core, a battery is an electrochemical cell for storing chemical energy and releasing it as electricity. This conversion is achieved through electrochemical oxidation-reduction (redox) reactions occurring at the cell's two electrodes. At the anode (negative electrode), oxidation takes place during discharge,

$$R \rightarrow O^{n+} + ne^{-} \tag{2.1}$$

where, R is a species donating n electrons to form an oxidized species O^{n+}. At the cathode (positive electrode), reduction occurs,

$$O'^{n+} + ne^{-} \rightarrow R'. \tag{2.2}$$

Separating them is the electrolyte, which conducts ions between the electrodes while forcing the electrons through an external circuit. For a battery to be rechargeable, this process must be reversible. [5]

During charging, an external energy input drives the electrochemical reactions in the non-spontaneous direction. Reduction will instead take place at the anode, and oxidation at the cathode. This is by design, energy is stored in a thermodynamically unfavourable state during charging, so that upon discharge the system can spontaneously relax towards equilibrium, releasing the stored energy as electrical work [1].

The thermodynamic driving force during discharge is a net decrease in the Gibbs free energy (ΔG) of the chemical species involved [26]. A reaction with a negative ΔG is spontaneous and drives electrons through the external circuit. The relationship between the Gibbs free energy change and the cell potential is given by

$$\Delta G = -zFE_{cell}, \tag{2.3}$$

where z is the number of electrons transferred and F is the Faraday constant (96 485 $\mathrm{Cmol^{-1}}$) [1].

The cell voltage E_{cell}, is determined by the difference in redox potentials of the two electrodes,

$$E_{\text{cell}} = E_{\text{cathode}} - E_{\text{anode}}. \tag{2.4}$$

An electrode with a lower redox potential will spontaneously donate electrons to one with a higher redox potential, defining the direction of current flow. [5]

From Liquid to Solid

In commercial lithium-ion batteries, reversibility is typically achieved through intercalation electrodes, such as graphite [2]. Yet intercalation chemistry carries an intrinsic limitation, the incorporation of a host lattice will contribute to added weight and volume beyond that the active material itself [27]. The total energy stored in an electrochemical cell can be determined by the average cell voltage during discharge and the total charge stored in the cell (i.e. the capacity). However, the gravimetric energy density of the cell is the energy stored divided by the total weight of the cell. Replacing the intercalation anode with a pure lithium metal anode would significantly increase the gravimetric and volumetric energy density [12, 13]. Lithium metal anodes can be used with the same type of cathode materials as in conventional lithium-ion batteries. In principle, lithium metal anodes can also be applied in batteries with conventional liquid electrolytes, however, they have a notoriously short cycle life due to dendrite growth and side reactions between the lithium metal and electrolyte [9, 14, 28]. To enable the adoption of lithium metal electrodes, it is therefore desirable to replace the electrolytes commonly used.

The discovery of highly lithium-ion conducting solid-state electrolytes (SSEs) has triggered a surge of interest in the solid-state battery (SSB) [16, 18]. The replacement of liquid electrolytes with a solid electrolyte eliminates the flammability and leakage risks inherent in organic solvent-based electrolytes used in conventional lithium-ion batteries [29]. This intrinsically safer configuration also enables a wider operating temperature range and avoids the gas build-up associated with electrolyte decomposition in liquid-electrolyte cells [30]. Solid-state electrolytes also offer a higher ionic transference number than their liquid counterparts. In liquid electrolytes, the mobility of counter-anions results in $\mathrm{Li^+}$ transference numbers well below unity, whereas in solid inorganic electrolytes the fixed anionic framework makes them single-ion conductors, driving the transference number close to unity [31–33]. This eliminates the anion concentration polarisation that limits electrode thickness in conventional cells, meaning that thicker electrode architectures become viable in solid-state batteries, opening a route to higher areal capacities [31, 34]. Moreover, according to the classic dendrite suppression theory by Monroe and Newman [17], SSEs with a shear modulus exceeding twice that of lithium metal should, in theory, suppress lithium dendrite growth.

A schematic comparison of a conventional liquid electrolyte lithium-ion battery and solid-state battery is illustrated in Figure 2.1. The most fundamental difference between the two configurations is the replacement of the liquid electrolyte with a solid one (highlighted in yellow in Fig. 2.1), which simultaneously eliminates the need for a separator, a component required in batteries with liquid electrolytes to prevent electronic short-circuiting between the electrodes. In solid-state batteries, this function is fulfilled by the electrolyte itself. Additionally, the graphite anode can be replaced by lithium metal to increase the energy density in solid-state battery cells.

In both cell concepts, the cathode is composed of an active material, a conductive agent, and typically a binder [35, 36]. In a conventional lithium-ion battery, only an electronic conduction pathway needs to be established within the cathode, as ionic conductivity is naturally ensured by infiltration of the liquid electrolyte into the porous electrode structure [5]. In a solid-state battery cathode, however, both ionic and electronic percolation must be simultaneously achieved throughout the composite electrode, placing significantly greater demands on its microstructural design [36].

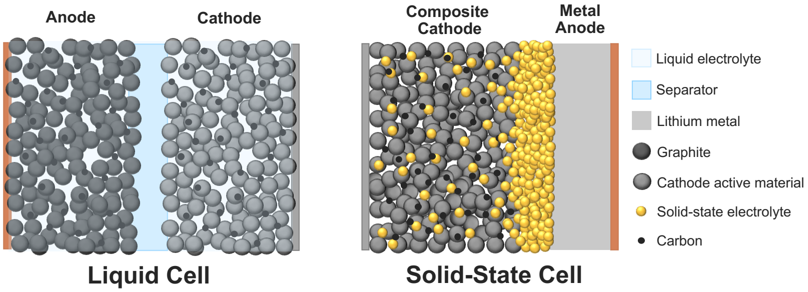

Figure 2.1: Schematic illustration of a conventional lithium-ion battery cell (left) and solid-state battery cell (right). Besides replacement of the graphite anode by a lithium metal anode, the most important difference between the cell configurations is the substitution of the liquid electrolyte (blue) by a solid-state electrolyte (yellow).

The SSE therefore plays a dual role, it acts as the lithium-ion conductor and as the physical separator between the anode and cathode. This multifunctionality is one of the architectural advantages of solid-state batteries, but it also introduces new complexity. Unlike liquid electrolytes, which wet electrode surfaces and can accommodate volume changes dynamically, solid electrolytes form rigid interfaces that are subject to coupled electrochemical, chemical, and mechanical processes. These electro-chemo-mechanical interactions at buried interfaces represent a critical distinction between solid-state batteries and conventional liquid electrolyte batteries, and their characterization presents experimental challenges [37].

The following sections introduce different classes of SSEs and cell configurations, with particular focus on the lithium metal anode. The interfacial phenomena outlined above, being both the central challenge and the primary research focus of this thesis, are treated in greater depth in **Chapter 3**.

2.1 Solid-State Electrolytes

An electrolyte is a material that conducts ions. If the ions move through a solid framework, it is a solid electrolyte, or solid-state electrolyte (SSE). In an electrochemical cell, the electrolyte serves as the medium through which ionic current flows between the two electrodes, completing the internal circuit while simultaneously preventing direct electronic contact between the electrodes [5]. This dual requirement, high ionic conductivity and negligible electronic conductivity, is a fundamental constraint any electrolyte must satisfy. Beyond the basic function of conducting ions, a practical electrolyte must fulfil a number of requirements for practical applications [33].

- **High ionic conductivity**, ensuring efficient ion transport at ambient and sub-ambient temperatures with minimal interfacial resistance.
- **Negligible electronic conductivity** to prevent internal short-circuiting and self-discharge.
- **Chemical stability** against the electrode materials, as well as moisture and oxygen, ensuring long-term compatibility throughout the cell lifetime.
- **Wide electrochemical stability window**. The electrolyte must remain chemically inert across the full range of electrode potentials it is exposed to, without oxidising or reducing at the cathode or anode interface, respectively.
- **Practical and environmental compatibility**. The electrolyte should be comprised of abundant and non-toxic materials, scalable and cost-efficient synthesis routes, and environmental compatibility for large-scale applications.

And specifically for a solid-state electrolyte,

- **Mechanical integrity**. The electrolyte must have sufficient mechanical stiffness to suppress lithium dendrite propagation while also maintaining good interfacial contact with the electrodes despite any volume changes associated with cycling.

A wide range of solid-state electrolytes have been developed so far [38]. It is important to recognize that, as of yet, no single material perfectly satisfies all of these criteria. The different types of SSEs available today can be broadly categorized into **organic** and **inorganic** electrolytes, although intermediate approaches such as solid-liquid hybrid electrolytes have also been explored [39]. These hybrid systems fall outside the primary scope of this thesis. Within the main material classes, several distinct families can be identified. Each of these presents its own set of advantages and challenges, and only a limited subset, primarily sulphides, oxides, polymers, and halide-based electrolytes, are currently commercially available, often at relatively high cost. [38, 40]

The following sections provide an overview of these electrolyte families, highlighting the key limitations associated with each class in the context of implementation in solid-state batteries. Particular attention is given to lithium argyrodite Li_6PS_5Cl (LPSC), which is the electrolyte investigated in this thesis.

Polymers
Polymer electrolytes are the most common class of organic solid-state electrolytes, with polyethylene oxide (PEO) being the most widely studied material [33]. Compared to inorganic electrolytes, they offer important advantages such as mechanical flexibility, enabling good interfacial contact with electrodes and low interfacial resistance. However, their main limitation is their low ionic conductivity at room temperature ($10^{-7} - 10^{-4}$ Scm^{-1}) [33, 41]. Therefore, most polymer electrolytes have to be used at high temperatures. Increasing salt concentration can enhance conductivity, but often reduces mechanical stability and flexibility [42]. Furthermore, PEO-based electrolytes demonstrate an electrochemical stability window up to 3.9 V vs. Li^+/Li, which makes them unsuitable for use with cathodes operating at higher cut-off voltages, such as LCO which exceeds 4.2 V vs. Li^+/Li [43].

Oxides
Oxide-based SSEs are a group of inorganic materials that can be categorized into various subtypes, such as garnet-type, (anti-)perovskite, NASICON or LISOCON, and LiPON-type, each with their distinct structural and electrochemical characteristics [44]. In general, oxide-based SSE exhibit good ionic conductivity ($10^{-4} - 10^{-3}$ Scm^{-1}) [33], but are mainly attractive due to their stability against lithium metal and their wide electrochemical stability window (0-6 V vs. Li^+/Li) [38, 45, 46]. The interface between the electrolyte and electrodes is one of the main problems of oxide electrolytes [47]. The electrolyte is stiff and brittle, resulting in poor interfacial contact. Moreover, oxide electrolytes face processing challenges due to their high sintering temperatures [38].

Halides
Halide-based SEEs have emerged as a promising class of inorganic materials due to their high ionic conductivity compared to oxides and polymer electrolytes, and their ductility [48–50]. The primary limitation of halide SSEs lies in their stability toward the Li metal electrode [48]. Due to having a low reduction potential, halides are reduced even upon contact with lithium [51]. However, their high stability against oxidation makes them suited for use with high-voltage cathode materials.

Sulphides
Sulphides, have attracted significant attention due to their high ionic conductivity ($10^{-3} - 10^{-2}$ Scm^{-1}), as a result of the larger atomic radius and lower electronegativity of sulphur reducing the Li^+ binding energy [33, 52]. Based on crystallinity, sulphide SSEs are categorized into three classes, glassy/amorphous, glass-ceramic, and crystalline [53, 54]. Moreover, sulphide SSEs exhibit favourable mechanical strength and flexibility compared to oxides. Their ductility and low hardness can improve interfacial contact with electrodes. However, the main limitation of sulphides relates to their limited chemical (H_2S generation in contact with moisture) and electrochemical stability [23, 55–57].

2.1.1 Li_6PS_5Cl

Among sulphide-based solid electrolytes, lithium argyrodites of the type Li_6PS_5X (X = Cl, Br, I) have emerged as one of the most important sub-classes due to their high ionic conductivity ($10^{-3} - 10^{-2}$ Scm^{-1}) [19]. The high ionic conductivity of Li_6PS_5Cl (LPSC) originates from the presence of partially occupied and disordered lithium sites within the argyrodite structure, which enable fast lithium-ion transport through a three-dimensional network of face-sharing tetrahedral sites, further facilitated by the mixing of S^{-2} and Cl^- over shared crystallographic positions [19]. Compared to liquid electrolytes, ion transport in solid materials relies on defects such as vacancies and interstitials. The ionic conductivity is therefore governed by both the concentration of mobile charge carriers and their mobility, the latter being determined by the activation energy for ion hopping between available sites in the crystal structure [58]. However, it is important to consider ionic mobility as a function of carrier density, that is, lithium-ion density [59]. Liquid electrolytes typically exhibit a high lithium-ion mobility and a low amount of lithium per unit volume, whilst sulphides require up to two orders of magnitude more lithium to reach their high ionic conductivity.

However, Li_6PS_5Cl is not fully stable against lithium metal and can undergo reductive decomposition, forming products such as Li_3P, LiCl, and Li_2S [23, 60–62]. This interfacial instability will be discussed further in **Chapter 3** and is one of the main topics of this thesis.

2.2 Anode Configurations & Materials

In addition to differences in material selection, battery electrodes can vary significantly in their design, physical properties, and operating mechanisms. While the cathode largely determines the achievable specific energy in solid-state batteries, due to its comparatively low specific capacity and the need for thick electrode architectures, the choice of anode remains critical. Overall, the selection and design of anode materials in solid-state batteries must balance several competing factors, including energy density, mechanical stability, and interfacial compatibility.

A wide range of anode architectures have been investigated for solid-state batteries, including lithium metal, and lithium-free anode alternatives such as insertion anodes and alloying anodes (see Fig. 2.2) [13, 63–65]. Carbon-based anodes, such as graphite, operate primarily via lithium-ion insertion mechanisms. These materials exhibit relatively small volume changes during cycling [66] but exhibit comparatively low specific capacity. Alloy-based anodes, such as silicon, offer significantly higher theoretical capacities [63]. However, silicon will undergo severe volume expansion during charging (lithiation) and discharging (delithiation), which remains a key challenge, particularly in the context of solid electrolytes, where mechanical constraints are more severe.

Another important strategy in solid-state battery design involves the engineering of the anode/solid electrolyte interface. Interfacial instability is a major limitation in solid-state systems, as poor physical contact and chemical reactions at the interface can lead to increased resistance and performance degradation [15]. To address this, interlayers can be introduced to improve interfacial contact, suppress side reactions, and promote more uniform lithium deposition and stripping [67–73].

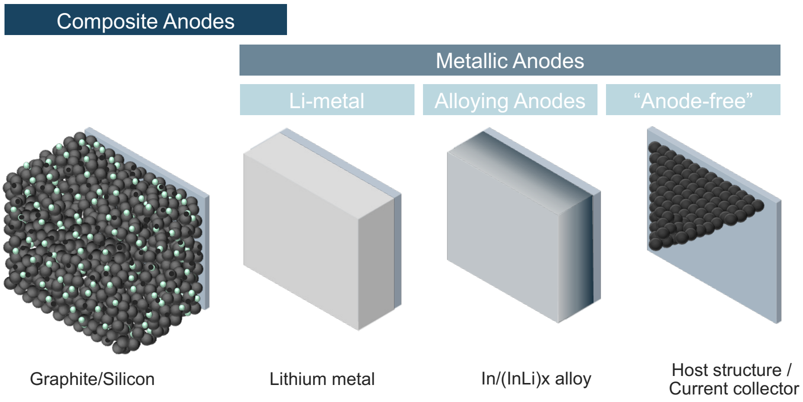

Figure 2.2: Schematic overview representing different anode architectures for solid-state batteries, including composite anodes (graphite, silicon), alloying-type anodes (Si, In), excess lithium metal, host structures or interlayers, and anode-free designs.

2.2.1 Lithium-metal

Lithium metal is the optimum anode material in terms of gravimetric and volumetric energy density [12, 13]. A good anode for high energy density batteries should combine high capacity per unit weight with a low electrochemical potential. Lithium satisfies both criteria, its low atomic weight and the absence of the need for a host material maximize the capacity per unit weight, while it possesses the most negative standard electrode potential of all metals [12]. Numerically, lithium metal has a theoretical specific capacity of 3860 mAh/g and a redox potential of -3.04 V vs. the standard hydrogen electrode, making it the ideal anode for high energy density batteries.

However, as an alkali metal, lithium is extremely reactive and highly sensitive to moisture and air, imposing strict requirements on how to be handled and demanding high electrochemical stability from any electrolyte it is paired with. During discharge, oxidation occurs at the anode,

$$\mathrm{Li} \rightarrow \mathrm{Li}^{+} + \mathrm{e}^{-}, \tag{2.5}$$

where metallic lithium donates an electron to release a lithium ion into the electrolyte. During charging the reverse reaction occurs, and lithium ions are reduced and electrodeposited as metal. This means the lithium anode is repeatedly dissolved and re-formed with cycling.

This repeated electrodeposition is one of the main practical challenges associated with the lithium metal anode. Despite appearing simple at first glance, the interfacial kinetics of a parent metal electrode such as lithium on a solid electrolyte is fundamentally complex, charge transfer is directly coupled to either crystal growth or dissolution, and the heterogeneous kinetics depend critically on the micro- and nanostructure of the growing or dissolving metal and the solid metal/solid electrolyte interface [13]. Overcoming the electrochemical and mechanical challenges of the lithium metal anode therefore requires a comprehensive understanding of interfacial processes, kinetics, and morphology, which will be discussed further in **Chapter 3**.

2.2.2 Anode-free Lithium-metal Batteries

Usually, lithium metal solid-state batteries are assembled using a SEE, a cathode composite, and a lithium metal anode (see Fig. 2.1). However, as cathode active materials are manufactured in a lithiated (discharged) state, the lithium foil on the anode adds unnecessary weight and volume since the cell cannot be further discharged [64, 67, 74, 75]. Therefore, reservoir free, or anode-free, cells are assembled with a metal current collector (CC) on the anode side, i.e. removing the excess lithium to further increase the energy density. The lithium anode is instead formed in the first charging step by delithiating the cathode active material as depicted in Figure 2.3.

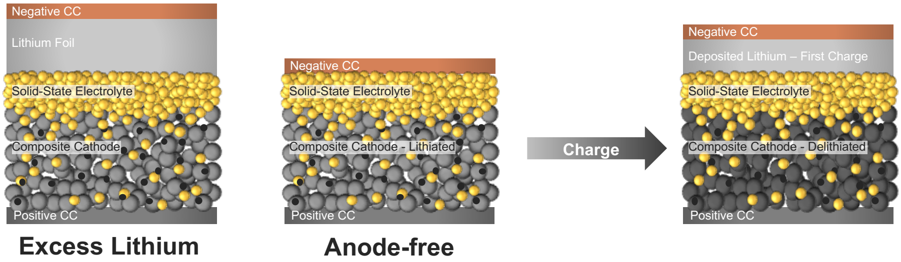

Figure 2.3: Schematic illustration of (left) excess lithium cell design using a lithium metal-foil providing a lithium reservoir during cycling in contrast to (middle) the anode-free configuration where no lithium metal is present at the anode side after assembly, reducing the cell volume and mass. Upon charging (right), lithium is deposited onto the current collector surface as the cathode active material delithiates.

Moreover, the need to handle lithium metal is omitted, which introduces practical benefits. Lithium will always react with the surrounding atmosphere due to trace amounts of atmospheric gases such as nitrogen, oxygen, water, and carbon dioxide, forming a resistive passivation layer [76]. Not only is it more practical and cost-effective to circumvent the handling of lithium foils, it is additionally safer due to its highly reactive nature.

While the anode-less concept offers advantages in terms of gravimetric and volumetric energy density, it also introduces additional challenges related to lithium plating efficiency and interfacial stability [67]. Now that no excess lithium is present in the cell, lithium losses cannot be compensated by an excess lithium reservoir. Since small lithium losses to side reactions or contact loss directly lead to a reduction in capacity, the requirements for the efficiency and reversibility of the system are even higher for anode-free cells.

Chapter 3

Interfaces & Interphases

The interface between the lithium metal anode and the solid-state electrolyte (SSE) has to fulfil several requirements in order to meet the performance goals motivated by the introduction of lithium metal.

- **The interfacial resistance** between lithium metal and the solid state electrolyte needs to be low and stable.
- **No loss of active material** (lithium) should take place, all processes and reactions must be fully reversible.
- **Morphological stability** during current load. Only once the interface is morphologically stable, stable electrochemical operation can be achieved.

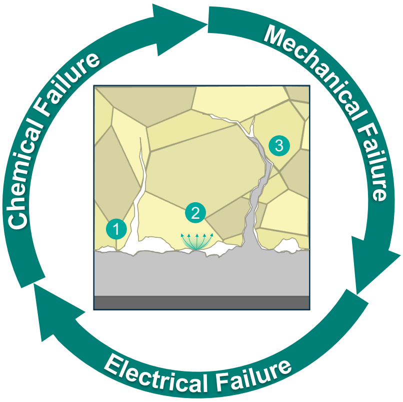

Figure 3.1: Illustration highlighting the coupled electro-chemo-mechanical processes occurring at the lithium metal/solid-state electrolyte interface.

These criteria require that a variety of thermodynamic, kinetic, and morphological properties of the lithium metal/solid electrolyte interface are well understood. Coupled electro-chemo-mechanical processes like the (1) mechanical degradation such as contact loss and cracking of the solid-state electrolyte, (2) electrochemical instability causing side reactions and interphase formation, and (3) non-uniform lithium morphology as well as dendrite formation, all govern the cell performance and failure. These buried, multi-scale processes (Fig. 3.1) are difficult to probe with conventional techniques. In this chapter we will discuss the instability of the lithium metal/SSE interface, both morphological and (electro)chemical.

3.1 Lithium Deposition, Morphology & Dendrite Formation

The lithium metal anode offers many advantages, as discussed in **sub-section 2.2.1**, but realizing this potential is complicated by the highly non-uniform nature of lithium electrodeposition [9, 12, 13]. Rather than plating as a smooth film, lithium forms and grows in a variety of microstructures depending on the substrate, electrolyte, current density, and applied pressure.

Nucleation & Deposition

Lithium deposition begins with nucleation once the local overpotential exceeds the surface energy barrier for forming a new phase [5]. The Gibbs free energy change for nucleation balances the bulk crystallization energy gain against the surface energy cost. Since these scale differently with nucleus size, there exists a critical radius below which nuclei are unstable and dissolve [77]. The overpotenital has been correlated with the size of the deposited nuclei. The electrochemical signature of this process is a characteristic voltage dip during plating, the nucleation overpotential (Fig. 3.2), which reflects the energy barrier that must be overcome to form stable nuclei. Once nuclei exceed the critical radius, growth proceeds and the potential relaxes.

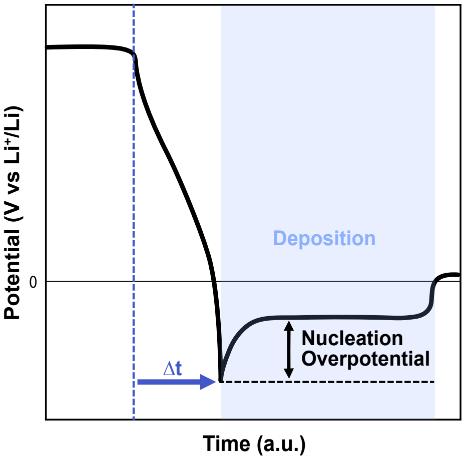

Figure 3.2: Schematic voltage profile during nucleation and subsequent shift of the nucleation peak due to parts of the applied current sustaining kinetically driven decomposition of the electrolyte.

In practice, the situation is not as ideal. Due to the low redox potential of lithium and narrow thermodynamic stability window of many electrolytes, electrolyte decomposition and lithium nucleation are not strictly sequential processes and can occur simultaneously. In this situation, a fixed current, typically used in a galvanostatic experiment, can be sustained by electrolyte degradation, and nucleation does not need to happen at the particular rate corresponding to the applied current during the deposition step [77]. This results in a shift of the nucleation peak in the voltage profile schematically presented in Figure 3.2.

The deposition rate and resulting nucleation density are influenced by the applied current density [67, 78, 79]. Increased overpotential at higher current densities results in a greater number of nuclei distributed across the current collector, which promotes uniform lithium coverage and, as plating progresses, potentially finer-grained deposits [67, 80]. Surface irregularities on the substrate in which lithium nucleates further concentrate the local current density, creating preferential sites for deposition that contribute to non-uniform growth [67]. The crystal structure of deposited lithium, grain size, and orientation, have also emerged as important parameters. Fuchs et al. [81] used focused ion beam and electron backscatter diffraction to reveal the microstructure of deposited lithium metal. They found that the microstructure was not only inherently different for electrodeposited metal compared to its metal-foil counterpart but also influenced by the current density, capacity, and pressure.

Dendrite Propagation & Cracking

Unstable lithium deposition can result in dendrite formation. Monroe and Newman predicted that a SSE with roughly twice the shear modulus of lithium (G_{Li} >6 GPa) could mechanically suppress dendrite growth [17]. However, despite the use of a SSE with a shear modulus higher than that of lithium, dendrites have been observed to mechanically penetrate through the bulk of the solid electrolyte and short-circuit the cell [82, 83].

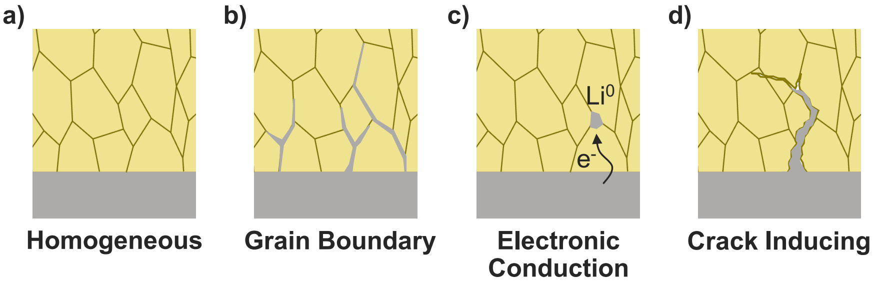

Figure 3.3: Schematic illustration of different lithium deposition and growth modes in solid-state batteries. a) Homogenously deposited lithium, the ideal morphology. b) Deposition and growth through grain boundaries. c) Deposition in the bulk of the solid-state electrolyte. d) Crack-inducing lithium deposition.

Dendritic growth can be initiated at interfacial irregularities such as surface roughness or defects, where local current concentration creates preferential sites for deposition [67]. However, dendrite initiation is not only governed by interfacial microstructure. In solid-state systems, two additional growth modes are illustrated in Figure 3.3. First, lithium preferentially deposits and propagates along grain boundaries in polycrystalline SSEs (Fig. 3.3b), driven by their inherently different ionic conductivity and mechanical properties compared to the bulk material, offering lower resistance pathways for filament propagation [82, 83]. Second, and more uniquely to solid-state systems, lithium can nucleate directly within the bulk of the SSE (Fig. 3.3c). This occurs because solid electrolytes possess a finite electronic conductivity, allowing electrons to reduce Li^+ ions in the electrolyte rather than exclusively at the electrode interface, leading to internal lithium deposition [84–86].

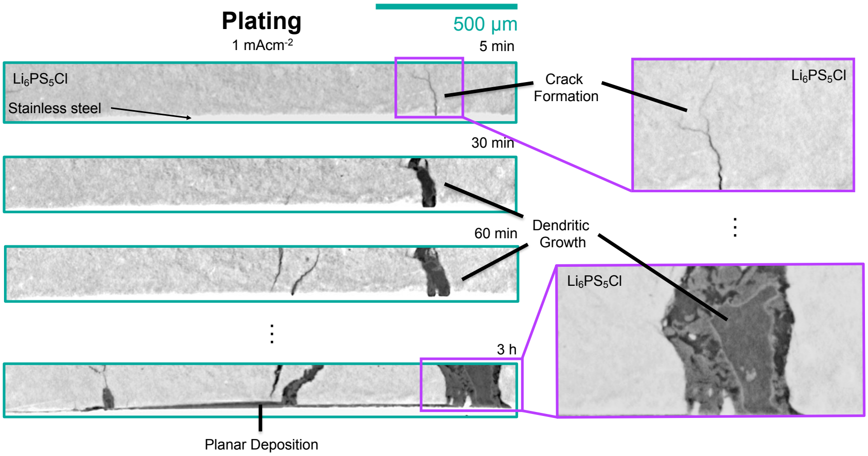

Figure 3.4: *Operando* X-ray μCT of lithium deposition in a stainless steel/LPSC/lithium metal cell at 1 mAcm^{-2}. Vertical cross-section at 5, 30, 60 minutes and 3 hours of deposition, showing the evolution of lithium morphology over time. In the early stage (5 min.), a crack initiates at the stainless steel/electrolyte interface. As deposition progresses, the crack widens and dendritic lithium grows in it, while planar deposition at the electrolyte/current collector interface is simultaneously observed. Zoomed insets show the crack after 5 minutes and the dendritic lithium structure within the crack after 3 hours.

Due to the preferential nucleation and accumulation of lithium at interfacial flaws and defects, mechanical stress is generated in the surrounding SSE, which can cause fracture [82, 87, 88]. Once cracks have formed, continued deposition and the applied stack pressure drive localized lithium growth in the cracks, simultaneously widening the crack and providing a low-resistance pathway for further dendritic growth (Fig. 3.3d). This creates a self-reinforcing cycle, deposition causes cracking, and cracking enables further deposition. This specific failure mode is further determined by the properties of the SSE itself, such as porosity. This process can be observed in Figure 3.4, showing a vertical cross-section of a stainless steel/LPSC/lithium metal cell during deposition from X-ray computed tomography. The time sequence reveals that in the early stages of deposition, a crack initiates at the interface between the stainless steel current collector and the electrolyte. As deposition continues, the crack widens and dendritic lithium growth proceeds, driven by the mechanical wedging force of the deposited metal. Notably, planar deposition at the electrolyte/current collector interface can also be observed simultaneously, highlighting the coexistence of different lithium deposition modes.

3.2 Lithium Stripping, Void Formation & Contact Loss

During lithium stripping, the oxidation of lithium metal at the lithium metal/SSE interface forms vacancies in the metal [89]. When the applied current density exceeds a critical threshold, where the diffusive flux of vacancies away from the interface into the bulk metal can no longer keep pace with the rate of generation, and vacancies accumulate and coalesce into voids at the interface [13, 90]. To put the relevant length scales in context, assuming completely homogeneous deposition, 3 mAhcm^{-2} of lithium corresponds to a layer thickness of approximately 40 μm, and this entire volume must be removed during stripping.

The consequences of void formation extend beyond simple contact loss. Voids increase the interfacial resistance [91] and create local current constrictions at the remaining contact points, which promote non-uniform deposition during subsequent plating and can act as nucleation sites for dendrites [92]. Void evolution is also dynamic over cycling [93], voids expand laterally during stripping but partially close during plating as lithium is re-deposited [94]. However, the closed off voids reopen in subsequent stripping cycles, leading to a gradual accumulation of contact loss and rising impedance over the lifetime of the cell.

External stack pressure is believed to counteract void formation by driving lithium creep at the interface. Lithium is highly ductile at room temperature and therefore susceptible to plastic deformation under moderate pressures [92, 93, 95]. The critical pressure required to suppress void formation is current-density dependent, and Wang et al. [95] proposed values of approximately 2.0 MPa needed at 400 μAcm^{-2}, while Kasemchainan et al. [92] suggest 7 MPa at 1 mAcm^{-2}.

Physical Contact Loss or Ionic Contact Loss
A common battery failure mode is a large rise in interfacial resistance during discharge, widely attributed to a cumulative loss of physical contact between the lithium metal and the SSE due to void formation. The current working hypothesis is that voids initiate and grow by vacancy condensation at the interface. This has been challenged on theoretical grounds by Roach et al. [96] who point out that there is no compelling driving force for vacancy nucleation and diffusion during one-dimensional stripping on the micron scale, even if vacancy aggregation may occur at the nanoscale involving small vacancy clusters and that conventional power law creep theory suggests that pressures of only 1–2 MPa should be sufficient to collapse voids in lithium.

It is also worth noting that much of the experimental evidence for void formation is indirect, inferred from increases in polarization or impedance during electrochemical characterization [90, 91]. However, such signatures do not directly indicate a loss of physical contact due to void formation. An alternative source of increasing interfacial resistance is the formation of resistive interphases at the lithium metal/SSE interface. While interphase formation is commonly assumed to be spatially homogeneous wherever physical contact exists [13, 55], localized or heterogeneous electrochemical degradation of the SSE or electrode could produce spatially non-uniform interphases (see Fig. 3.5). Such inhomogeneous interphase formation could produce electrochemical signatures, such as rising impedance, and increased polarization, indistinguishable from those attributed to void formation. Disentangling these two contributions remains an open challenge and is discussed further in **Chapter 6** and the results from **Paper II**.

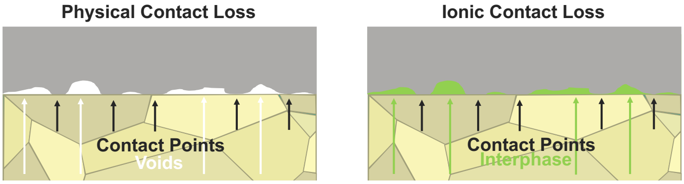

Figure 3.5: Schematic illustration of two distinct mechanisms of interfacial contact loss at the lithium/SSE interface. (Left) Loss of physical contact due to void formation leaving regions with no physical or electrochemical contact between the lithium metal and the SSE. (Right) Loss of contact due to heterogeneous interphase formation.

3.3 Reactivity & Interphase Stability

The interface between the lithium metal anode and the SSE is not merely a geometric boundary, but a region where significant chemical and electrochemical driving forces are present. Understanding whether and how the SSE reacts with lithium metal requires considering the relative energy levels across this interface.

In simplified terms, the electrochemical stability window is the voltage range between the reduction and oxidation limits of the electrolyte [1]. The position of the conduction band minimum (often considered as the lowest unoccupied molecular orbital), can give an *estimate* of the electrochemical stability against reduction of the electrolyte [13, 97]. If the Fermi level of lithium metal lies above the conduction band minimum of the electrolyte, electrons will spontaneously transfer from the metal into the electrolyte, reducing the SSE and driving interphase formation. The SSE will react with lithium either chemically, driven by the thermodynamic instability, or electrochemically during cell operation when current flows and the interface potential is further polarized.

The product of these reactions is an interphase layer, a chemically distinct region that grows between the lithium metal and the SSE. How the resulting interphase is classified is determined by its transport properties further discussed in **sub-section 3.3.1** as well as the specifics of the interphase formed discussed in **sub-section 3.3.2**.

3.3.1 Interphase Classification

Following the framework established by Wenzel et al. [55], three types of Li/SSE interfaces can be distinguished based on the thermodynamic and kinetic nature of the interfacial reaction.

Thermodynamically Stable Interface
In this ideal case, no interphase forms because either there is no thermodynamic driving force for reaction between lithium and the SSE, or the reaction kinetics are so slow as to be negligible on practical timescales. The interface remains sharp and chemically unchanged during cycling. Few SSE materials satisfy this condition in contact with lithium metal [22].

Reactive Interface - Mixed-Conducting Interphase
Here the SSE reacts with lithium to form an interphase that conducts both ions and electrons. Because electrons can pass through the mixed-conducting interphase, further reduction of the SSE can take place, and the interphase grows continuously. This progressive growth consumes active electrolyte and electrode material, increases cell resistance, and can ultimately lead to cell failure. This is the most detrimental case.

Kinetically Self-limiting Interface - Passivating Interphase
The SSE reacts with lithium, but the reaction products are predominantly ionically conductive and electronically insulating. The interphase therefore passivates the interface. Once a sufficiently thick layer has formed, or if none of the decomposition products are electronically conductive, electron transfer from the lithium metal to the SSE is blocked and further reaction is suppressed. This represents the most practically tolerable form of interfacial reactivity, provided the interphase remains thin, mechanically stable, and homogeneously distributed.

3.3.2 Reactivity of Lithium metal / Li_6PS_5Cl Interfaces

Li_6PS_5Cl (LPSC) is thermodynamically unstable in contact with lithium metal. Based on first-principles calculations, Zhu et al. [22] predicted a reduction potential of 1.71 V vs. Li^+/Li and an oxidation potential of 2.01 V vs. Li^+/Li for LPSC, giving a relatively narrow electrochemical stability window. The expected reduction reaction produces binary lithium compounds according to [60, 98],

$$Li_6PS_5Cl + 8Li \rightarrow Li_3P + 5Li_2S + LiCl \tag{3.1}$$

where the reduction products Li_2S, Li_3P, and LiCl are thermodynamically stable against lithium metal. Hence, during chemical degradation, a multiphase layer is formed. When trying to classify the formed interphase, the transport properties need to be considered. Li_2S and LiCl are ionically conductive, but worse than LPSC, and exhibit a relatively low electronic conductivity [60]. However, Li_3P is a mixed ionic-electronic conductor [99]. On the one hand, beneficial ionic pathways (i.e., by Li_3P) may support the conduction of lithium ions, effectively bypassing regions with lower ionic conductivity (i.e., Li_2S and LiCl). On the other hand, the presence of Li_3P in the interphase also provides pathways for electrons to reach the reaction front between the interphase and fresh SSE, sustaining further reduction and continuous growth, characteristic of a mixed-conducting interphase. The resulting inhomogeneity creates a percolation pathway through the interphase, which could cause an inhomogeneous lithium-ion flux during cycling [60, 99].

The Li/LPSC interphase has been reported to grow following a square-root of time dependence consistent with a Wagner model for diffusion-controlled solid-state reactions [60, 62, 98, 99]. This has been used to estimate the interphase thickness to be on the order of a few hundreds of nanometres, approximately 315 nm after one week of contact [98]. This is consistent with results from time-of-flight secondary ion mass spectrometry, *in situ* X-ray photoelectron spectroscopy, and atomic force microscopy measurements [100, 101]. However, whether the interphase truly follows a simple Wagner-type growth, or what the rate-determining diffusion step is are at present unclear.

Recent work by Burton et al. [99] provided further insights into the growth process. Using a combination of electrochemical measurements and X-ray photoelectron spectroscopy, they identified a gradient of partially lithiated phosphorus species, Li_xP, throughout the interphase. They observed a gradient with more reduced species (Li_3P) near the lithium metal anode and less reduced species (Li_xP) near the SSE. This gradient arises because LPSC begins to reduce at potentials (1.71 V vs. Li^+/Li) well above the full reduction of Li_3P, forming intermediate Li_xP species (and Li_2S, LiCl, P), and full lithiation to Li_3P only occurs at 0.87 V vs. Li^+/Li. The proposed reduction order is as follows:

$$\text{At 1.71 V vs. Li}^+/\text{Li}: \quad \mathrm{Li_6PS_5Cl} \rightarrow \mathrm{Li_2S} + \mathrm{LiCl} + \mathrm{P} \tag{3.2}$$

$$\text{At 1.30 V vs. Li}^+/\text{Li}: \quad \mathrm{P} \rightarrow \mathrm{Li_xP} \tag{3.3}$$

$$\text{At 0.87 V vs. Li}^+/\text{Li}: \quad \mathrm{Li_xP} \rightarrow \mathrm{Li_3P} \tag{3.4}$$

This establishes a lithium chemical potential gradient across the formed interphase, from lithium metal through $Li_3P \rightarrow Li_xP$ toward the SSE, which drives coupled Li^+/e^- diffusion through the Li_3P phase. Lithium diffusion through the lithiated phosphorus is therefore the rate-determining step for the interphase growth. Importantly, this process continues at open-circuit potential, where chemically driven decomposition persists as long as metallic lithium and a continuous Li_xP percolation pathway are present. [99]

These findings from Burton et al. [99] imply that the diffusivity through the interphase is not constant but varies with the lithiation state of the phosphorus species, and may explain parts of the disagreements remaining in the literature regarding the long-term growth behaviour of the lithium metal/LPSC interphase [23, 24, 60, 98, 99, 101]. These discrepancies likely also reflect differences in operational conditions and are discussed more in **Paper I** and **Chapter 6** where the interphase growth kinetics was found to be dependent on the preconditioning, current density, and areal capacity.

3.4 Stack Pressure

From the various interfacial processes discussed, it is clear that stack pressure is an important parameter in solid-state battery operation. High pressure during preparation of the pellet is essential to achieve intimate solid–solid contact given the rigidity of inorganic SSEs [102]. Typically, for sulphide-based solid-state electrolytes, an average pressure of 300 MPa is used to densify the pellet [103]. Sustained operational pressure is required to counteract electrode volume changes during cycling and maintain interfacial contact. However, the pressures currently needed (10-70 MPa, [103]) are considered too high for practical industrial application [104], making pressure management an important engineering challenge.

The effects of stack pressure on the lithium/SSE interface are coupled to several of the processes discussed above. During stripping, pressure drives lithium creep, counteracting void formation and contact loss [96]. However, if the applied pressure is excessive, the creep can force lithium into cracks and defects in the SSE, propagating fractures and causing short circuits through a purely mechanical pathway, without requiring electrochemical dendrite growth [105].

At the electrode level, higher pressures promote denser and more uniform lithium deposits, reducing the active surface area exposed to the SSE and thereby limiting parasitic side reaction sites. Similarly, insufficient pressure prevents sufficient plastic deformation of lithium, resulting in poor physical contact at the interface and confining interphase formation to isolated contact points [106, 107]. The net result is that stack pressure simultaneously governs mechanical contact, lithium morphology, and interphase formation, making the lithium/SSE interface an inherently coupled electro-chemo-mechanical system.

3.5 Methods to Characterize the Interface

The processes occurring at the lithium metal/SSE interface span a wide range of length and time scales, from nanometre-thick interphase layers and grain boundaries to micrometre-sized voids and macroscopic cracks, making comprehensive characterization challenging. Measurements can be classified as *ex situ*, *in situ*, or *operando*, depending on whether the interface is characterized outside the cell, inside a resting cell, or during operation. *In situ* and *operando* approaches are preferable as they avoid mechanical and chemical alteration of the reactive lithium interface, though they typically require specialized cell designs [37, 108].

Scanning electron microscopy (SEM) is an imaging technique that is widely used in battery research [37]. SEM provides a greater spatial resolution than optical microscopy (down to several nanometers) but requires the sample to be inside a vacuum chamber. Due to the low penetration depth of electrons, SEM can only be performed on surfaces or at cross-sections after for example focused-ion beam milling (FIB). Pairing SEM with FIB is particularly advantageous for solid-state battery research due to the buried nature of the interfaces. Due to its destructive nature, FIB characterization is limited to *ex situ* evaluation of samples. Moreover, typical milled regions are tens of microns in width [37]. Another challenge with FIB-SEM is beam damage, as lithium alloys with Ga (typical ion-beam) which causes morphological and compositional changes to the interface. Sulphide SSEs such as LPSC can also show redeposition under Ga milling at room temperature. Cryogenic FIB can be used to minimize beam damage, but understanding potential artifacts that can arise from the milling process remains important to ensure that they do not affect data analysis. (Cryo)FIB-SEM has been used to image lithium morphology, and interphase formation in solid-state batteries[73, 93, 106].

Spectroscopic techniques such as X-ray photoelectron spectroscopy (XPS) and time-of-flight secondary-ion mass spectrometry (ToF-SIMS) offer chemical information and have been used to identify interphase composition and thickness [62, 100, 101]. Although XPS allows for both *ex situ* and *in situ* studies, the use of these techniques often requires cell designs that are quite different from standard lab cells [37]. ToF-SIMS also require exposing the sample for analysis, and is a destructive technique due to the ablation required for mass spectrometry [37].

Electrochemical methods, such as galvanostatic cycling, cyclic voltammetry and impedance spectroscopy, provide high temporal resolution and require no sample preparation. They can be used to assess the electrochemical stability and reversibility of the probed system, to quantify coulombic efficiency during cycling, and to track the evolution of interfacial resistances and transport processes over time [56, 61, 109]. However, their signatures are non-specific, and typically require knowledge about the studied system [37].

X-ray computed tomography (XCT) has been used to study solid-state batteries due to its non-destructive nature and ability to image buried features within a cell. The spatial resolution depends on the X-ray source and experimental setup, ranging from tens to hundreds of nanometres for nano-CT to tens of micrometres for micro-CT [37], making it suitable for imaging features across a broad range of length scales. Combined with *in situ* or *operando* cell designs, XCT has been particularly powerful for tracking morphological evolution during cycling, for instance, the initiation and propagation of lithium dendrites and cracks [82, 110, 111].

The primary contrast mechanism in XCT is the attenuation of X-rays by the sample. This makes XCT well suited for imaging high-contrast features, but provides limited chemical information and poor contrast between materials of similar density or atomic number. This is a particular challenge for lithium-containing systems, as lithium is a light element with very low X-ray attenuation, making it difficult to distinguish it from other low-density components. Strategies to address this limitation, for example combining tomography with other contrast mechanisms such as X-ray diffraction, are discussed in **Chapter 5**.

Given these complementary strengths and limitations, this thesis combines electrochemical characterization with X-ray based methods to study the lithium metal/LPSC system. These two approaches are introduced and discussed in detail in **Chapters 4** and **5** respectively.

Chapter 4

Electrochemical Characterization of Interfaces

Several important interfacial processes at the lithium metal/solid-state electrolyte (SSE) interface can be assessed through electrochemical characterization. As discussed in **Chapter 3**, the processes occurring at this interface, including interphase formation and growth, contact loss, and lithium deposition, all leave signatures in electrochemical observables such as changes in impedance and voltage. However, interpreting these signatures correctly requires a solid understanding of the electrochemical properties of the system. In this chapter, we introduce and discuss the electrochemical methods used in this thesis to study the lithium metal/Li_6PS_5Cl electrolyte interface.

4.1 Electrochemical Cell

The design of electrochemical cells for measurements of solid-state batteries is critical for obtaining accurate and reproducible results. Unlike liquid electrolyte batteries, where coin cells are commonly used due to their simplicity, solid-state cells require careful control of the stack pressure to ensure intimate solid–solid contact, both between SSE particles, and at the electrode/SSE interfaces (see **Section 3.4**). In coin cells, the internal pressure is governed by the compression of an internal spring [37]. Consequently, spring size, but also the stack thickness will affect the internal pressure on the cell stack, leading to poorly controlled and variable pressures, reported to range between 40 and 103 kPa [112], which is not only too inconsistent, but often too low compared to the stack pressure commonly used for solid-state batteries (in the range of a few to tens of MPa) [103].

The importance of pressure control for the reproducibility of electrochemical measurements of solid-state batteries has been highlighted by Puls et al. [103]. By providing the same battery material to multiple laboratory groups, and allowing them to assemble cells using their individual cell setups and processing protocols, a large variability in electrochemical performance was found, with differences in processing and stack pressure identified as a key contributing factors. This boils down to two important pressures to consider, the pressure used for densification of the SSE pellet, and the stack pressure used for cycling and electrochemical testing.

For inorganic SSEs, to create a self-standing pellet, sintering is typically used. One of the main advantages of LPSC is its ability to be ”cold sintered”, i.e.

densified using high pressures (>300 MPa) at room temperature [113]. The applied pressure is important to reduce residual void space and enhance the ionic conductivity by improving the grain boundary contact [113]. Both the applied pressure and compression time influence the cell performance [103]. Another important factor to consider is the particle size, and particle size distribution, of the SSE powder. Smaller particles optimize the charge transport properties and offer a higher interface area with the active material, in the case of a composite cathodes [114], whilst larger particles have been found to fracture during densification [113].

In this thesis, commercially available Li_6PS_5Cl from NEI Corporation was used, with a particle size of < 1 μm. All processing and assembly steps were performed inside the laboratory electrochemical cell (see Fig. 4.1). 250 mg of LPSC powder was loaded on top of the current collector (stainless steel disc, 13 mm diameter) and uniaxially pressed between two stainless steel plungers at approximately 440 MPa for 5 minutes to densify the SSE powder into a pellet.

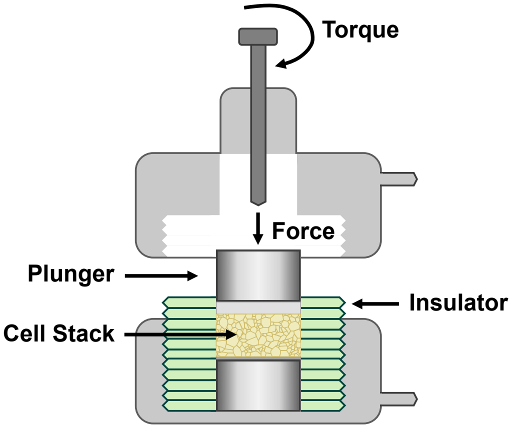

Figure 4.1: Schematic figure of cell for lab-scale electrochemical testing. Stack pressure applied by torque on the cell stack placed between two stainless steel plungers.

Following the densification step, lithium metal discs (300 μm, 10 mm diameter) were placed on top of the pellet. Two cell configurations were used in this work. In the symmetric configuration, lithium metal was placed on both sides of the SSE pellet, whereas in the asymmetrical configuration (anode-free) lithium metal was only placed on one side of the pellet serving as counter/reference electrode while the working electrode was the stainless steel current collector. A uniaxial stack pressure of approximately 10 or 30 MPa was applied during all electrochemical measurements.

How the stack pressure is applied is another important parameter. Two common approaches are constant pressure, where a defined force is maintained throughout cycling, for example using a spring, and through fixed volume, where the cell dimensions are constrained and the pressure evolves as the electrode stack expands and contracts during cycling [115]. In this thesis, the stack pressure was applied by torque, pressing the top plunger down onto the stack operating at approximately constant volume.

4.2 Galvanostatic Cycling

Galvanostatic cycling is one of the most widely used electrochemical methods to evaluate battery materials and full cells. A fixed current is applied between the counter electrode (CE) and the working electrode (WE), and the potential required to maintain this current is measured as a function of time or capacity [116]. The output is typically displayed as voltage vs. capacity or voltage vs. time (see Fig. 4.2), providing information about the reversibility, capacity, and stability of the electrochemical processes occurring at the electrodes.

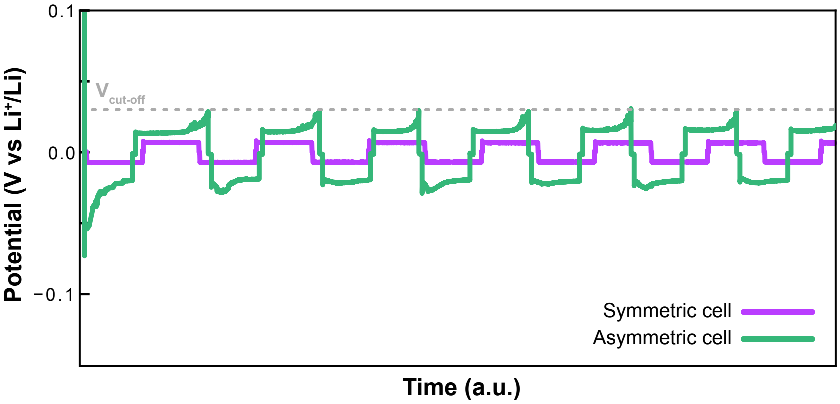

Figure 4.2: Galvanostatic cycling of a Li/LPSC/Li symmetric cell where each plating and stripping sequence is terminated when a set time has passed, compared to galvanostatic cycling of a SS/LPSC/Li asymmetric cell where the plating is terminated when a set time has passed, but the stripping is terminated at a cut-off voltage.

Two cell configurations have been used in this thesis to study the stability and reversibility of lithium metal anodes, illustrated in Figure 4.3. In the symmetric cell configuration, both electrodes are lithium metal foil. This setup is commonly used to assess the compatibility between the electrode and electrolyte, for example the tendency to short-circuit or to evaluate the impedance evolution during cycling or during chemical degradation at open circuit voltage [117, 118] (Fig. 4.5). Since both electrodes undergo the same reactions, any changes in cell voltage or resistance can be attributed to the electrode/electrolyte interface.

In the asymmetric or anode-free configuration, a lithium metal foil acts as the ion reservoir and CE, while the WE is a non-reactive metal such as stainless steel. This configuration is well suited for studying the efficiency of lithium plating and stripping through coulombic efficiency measurements [73, 119], as well as for evaluating the chemical stability between lithium metal and the electrolyte through coulometric titration time analysis (CTTA) [98], as described in **Section 4.4**.

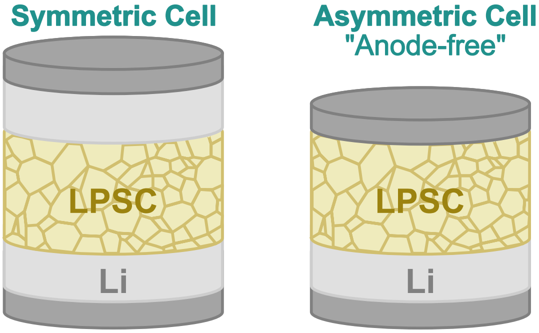

Figure 4.3: Cell configurations used. (Left) Symmetric cell, using two lithium metal electrodes, and (right) asymmetric cell with one stainless steel working electrode and one lithium metal counter electrode.

4.3 Electrochemical Impedance Spectroscopy

Electrochemical impedance spectroscopy (EIS) is a powerful technique for characterizing the electrical properties of materials and, in particular, the behaviour of interfaces within electrochemical systems. When a potential difference is applied across a heterogeneous system, each interface polarizes in a characteristic manner, leading to non-uniform charge distributions. The rate at which this polarization responds to changes in the applied signal depends on the nature of the interface. These differences in response times form the basis for distinguishing individual processes using EIS. [120]

Upon electrical perturbation, a multitude of processes occur simultaneously within the system, including electron transport through electronically conductive phases, charge-transfer reactions at electrode/electrolyte interfaces (oxidation and reduction processes), and ionic transport through the electrolyte [120]. The overall electrical response is governed by the combined contribution of these processes, as well as by the ohmic resistance of the electrodes and electrolyte. Additional impedance contributions may arise from microstructural features such as grain boundaries, secondary phases, and point defects, all of which can influence charge transport.

EIS probes these processes by applying a small sinusoidal perturbation, either in voltage or current, and measuring the corresponding response. By varying the frequency of the applied signal, processes occurring on different timescales can be resolved, fast processes dominate at high frequencies, whereas slower phenomena, such as diffusion or interfacial reactions, appear at low frequencies.

Working Principle

In a typical potentiostatic electrochemical impedance spectroscopy (PEIS) experiment, a sinusoidal voltage perturbation is applied to the system,

$$V(t) = V_m \sin(\omega t) \tag{4.1}$$

and the resulting current response is measured

$$I(t) = I_m \sin(\omega t + \theta) \tag{4.2}$$

where θ is the phase shift between the voltage and current signals (Fig. 4.4a). For purely resistive behaviour, $\theta = 0$, whereas deviations from zero indicate capacitive or inductive contributions. The ratio of the voltage to the current defines the impedance,

$$Z(t) = \frac{V(t)}{I(t)}. \tag{4.3}$$

Because both magnitude and phase information are retained, impedance is a complex quantity that can be expressed as

$$Z(\omega) = Z'(\omega) + iZ''(\omega) \tag{4.4}$$

where Z' and Z'' are the real and imaginary components, respectively. A significant amount of information about the system is acquired by varying the applied frequency in an EIS measurement. This data is commonly represented using Nyquist plots, where the imaginary component $-Z''$ is plotted against the real component Z' , often resulting in semicircular arcs that correspond to distinct electrochemical processes. Figure 4.4b shows the Nyquist plot for a model electrical circuit in which each data point represents one $Z(\omega)$ measurement. The circuit consists of a serial resistor R, and a resistor connected in parallel to a capacitor R/C.

At high frequencies, the impedance through the capacitor of the R/C element is much lower than through the parallel resistor, which is why the real impedance part $\mathrm{Re}(Z)$ dominates. In contrast, the current mainly flows though the resistor at low frequencies, resulting in a predominantly capacitive impedance response $\mathrm{Im}(Z)$. So, when the frequency is high, the impedance is equal to the serial resistance R. The left hand side of the Nyquist plot represents the high frequency impedance, and the distance from the origin to the high frequency data points is equal to the serial resistance. Conversely, on the opposite side of the semicircle is the low frequency impedance data. At very low frequencies, or close to zero, the impedance is equal to the sum of both the serial and parallel resistance. Based on the high frequency data we know that this is the distance from the origin to the left hand side of the semicircle. This means that the width of the semicircle is equal to the parallel resistance.

The frequency at the apex of the semicircle in the Nyquist plot gives an estimate of the time constant associated with the conduction process,

$$\tau = RC. \tag{4.5}$$

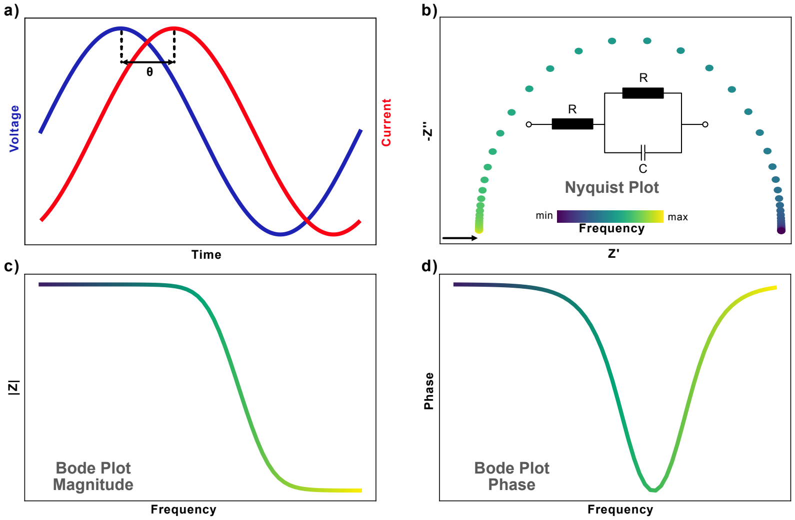

Figure 4.4: a) Sinusoidal voltage input at a single frequency and current response with resulting phase shift. b) Nyquist plot of an impedance spectrum simulated for the model electrical equivalent circuit shown in the centre of the plot. c) Bode plot of the magnitude of the impedance and d) phase angle against frequency.

Hence, one semicircle corresponds to one single electrochemical time constant, typically arising from a combination of charge-transfer resistance and double-layer capacitance at an electrode-electrolyte interface. And the example of a resistor in series with a parallel R/C element is commonly used to model dielectric materials and determine SSE conductivity using ion-blocking electrodes. [118]

The Nyquist plot it typically presented with complementary Bode plots. They are contain the same data, i.e., $\mathrm{Re}(Z)$ and $\mathrm{Im}(Z)$, but in a Bode plot the magnitude of Z,

$$\mid Z(\omega) \mid = \sqrt{\mathrm{Re}(Z(\omega))^2 + \mathrm{Im}(Z(\omega))^2} \tag{4.6}$$

and the phase angle θ,

$$\theta(\omega) = \tan^{-1} \frac{\mathrm{Re}(Z(\omega))}{\mathrm{Im}(Z(\omega))}. \tag{4.7}$$

are plotted as function of frequency and therefore allowing direct visualization of frequency-dependent behaviour [120].

In the Bode representation, the magnitude $\mid Z \mid$ of the impedance vs. frequency (Fig. 4.4c) exhibits a plateau followed by a decay which shows the transition from impedance being dominated by sum of both the serial and parallel resistance at low frequencies to just the serial resistance at high frequencies.

Similarly, the phase angle θ vs. frequency (Fig. 4.4d) exhibits a negative peak around the characteristic frequency (apex of the semicircle), reflecting the capacitive response of the parallel R/C element.

Analysis

The key feature of EIS is that the frequency-dependent measurements provide access to the characteristic relaxation times of different physical and chemical processes. In practice, electrochemical systems exhibit a distribution of relaxation times arising from structural and chemical heterogeneities, meaning that in a solid-state battery multiple resistance contributions are expected to appear across the frequency spectrum. At the highest frequencies, bulk ionic conduction through the solid electrolyte dominates the response, while at intermediate frequencies charge-transfer processes at the cathode and anode interfaces become distinguishable. At the lowest frequencies, solid-state lithium diffusion within the electrode materials governs the response. [121]

In real systems such as solid-state batteries, all of these processes can occur simultaneously, and those with similar time constants will overlap, producing complex and convoluted spectra in the Nyquist plot. While a single well-resolved semicircular arc can yield quantitative estimates of resistance and capacitance for a given process, deconvoluting contributions with similar time constants presents a significant challenge. This is illustrated in Figure 4.5, which shows EIS measurements collected continuously over time on a symmetric Li/LPSC/Li cell at open circuit voltage (OCV). At OCV no current flows, and any observed changes can be attributed directly to the chemical reaction between lithium metal and the SSE.

Three distinct semicircles are visible in the Nyquist plot, corresponding to contributions at high, intermediate, and low frequencies respectively. As time progresses, a shift in the real axis intercept is observed alongside the evolution of the individual semicircles. Crucially, not all contributions evolve equally, the Bode plot of the phase angle reveals that the high- and low-frequency contributions become progressively more negative with time, while the intermediate-frequency contribution changes comparatively little. This frequency-resolved view demonstrates that the growing interfacial resistance is not simply a uniform scaling of all processes but reflects the selective evolution of specific contributions associated with the interphase formation at the lithium/LPSC interface. This kind of qualitative inspection of both Nyquist and Bode representations can therefore reveal which processes are most affected by a given degradation mechanism, even without detailed quantitative modelling.

The conventional approach to quantitative analysis is to model the electrochemical system as an equivalent circuit model (ECM), in which resistors, capacitors, and other elements are fitted to represent a specific electrochemical phenomena. However, since no solution to an impedance spectrum is unique and the addition of more circuit elements will tend to improve the fit regardless of physical justification, ECM construction relies heavily on knowledge about the system and can be highly subjective [118, 122, 123].

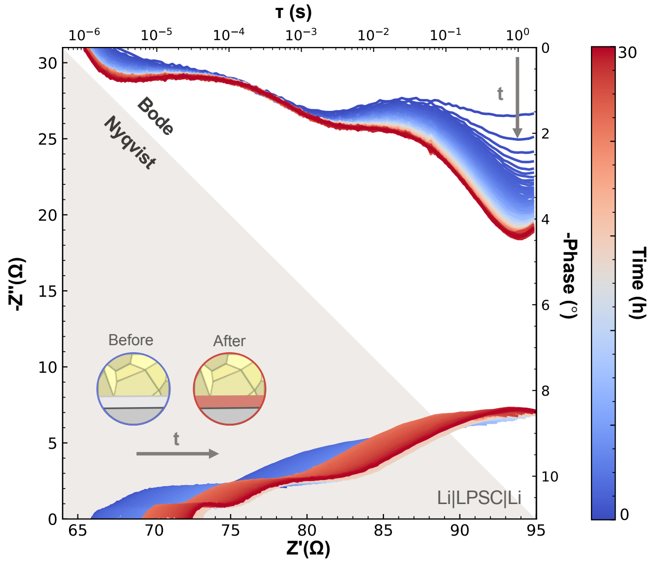

Figure 4.5: Electrochemical impedance spectroscopy of a symmetric Li/LPSC/Li cell over 30 hours at open circuit voltage showing the Nyquist plot and Bode plot with negative phase angle plotted against relaxation time ($\tau = 1/2\pi f$). The progressive evolution of the impedance spectra reflects the chemical instability of the Li/LPSC interface.

To address the limitations of equivalent circuit models, the distribution of relaxation times (DRT) method has emerged as a complementary tool for EIS analysis. Unlike model-dependent fitting, DRT is a technique that transforms frequency-domain impedance data into a time-domain distribution of characteristic timescales such that peaks associated with distinct characteristic time constants become directly visible [122, 123].

While DRT has its advantages over ECM fitting, it comes with several inherent limitations. The choice of kernel function constrains the analysis to a predefined transfer function type, typically a resistive–capacitive element, limiting the range of describable phenomena. Since most electrochemical systems are nonlinear, small-signal perturbations are required for valid impedance measurements, which in turn degrades the signal-to-noise ratio and risks masking low-polarization processes. Most DRT methods rely on solving an ill-posed optimization problem, meaning that the necessary regularization introduces a degree of freedom that compromises the uniqueness of the resulting distribution. Furthermore, regularization acts as a low-pass filter on the distribution function, broadening peaks and making it difficult to resolve processes with similar time constants. Finally, all current DRT formulations assume a serial arrangement of elementary transfer elements, meaning that parallel electrochemical processes cannot yet be adequately represented. [118, 124].

Ultimately, the most appropriate analysis strategy depends on the complexity of the system and the specific information sought. In some cases, full ECM fitting or DRT deconvolution is necessary to quantitatively separate overlapping contributions, while in others, qualitative inspection of the Nyquist and Bode plots alone is sufficient to identify meaningful changes, such as evolution of semicircle size, position or emergence, without the need for detailed modelling.

4.4 Coulometric Titration Time Analysis (CTTA)

Coulometric titration time analysis (CTTA), introduced by Aktekin et al. [98], offers a complementary approach to quantify interphase growth by tracking the progressive increase in lithium consumption time across successive titration steps, providing a measure of the total charge consumed by side reactions as a function of time.

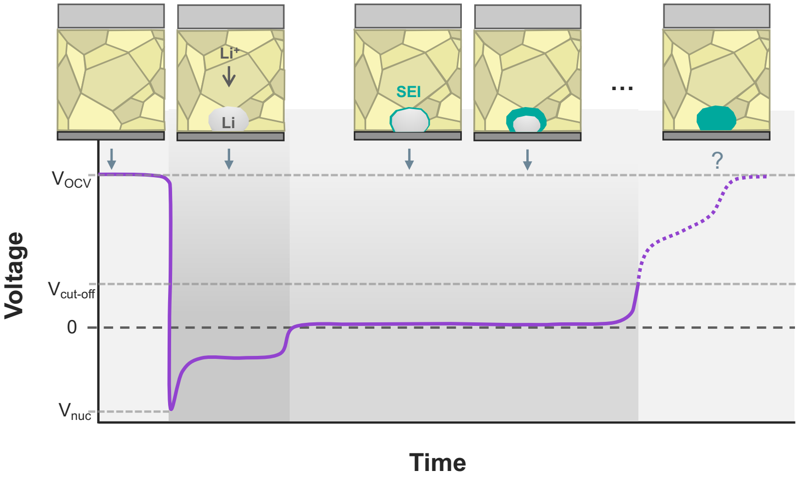

Figure 4.6: Schematic illustration inspired by [98] visualizing the coulometric titration of lithium metal onto the current collector and its gradual consumption by side reaction during the following OCV period, marking the time analysis step of the sequence. The formation of an interphase (SEI) is marked in green. The sequence ends when all lithium is consumed, defined by a voltage increase and cut-off leaving the full relaxation of the voltage profile unexplored.

Working Principle

CTTA is performed in an anode-free asymmetric cell configuration (see Fig. 4.3). As lithium metal is only present at the CE, the cell OCV is >0 V vs. Li^+/Li prior to any deposition. The technique operates through a repeated sequence of lithium deposition and OCV steps. Each titration step consists of a galvanostatic deposition of a small, controlled amount of lithium, typically in the range of a few μAhcm^{-2} [98], onto the current collector (CC), followed by an OCV period during which the deposited lithium is consumed by interfacial side reactions (Fig. 4.6). In an ideal limiting case, a perfectly stable electrolyte with no side reactions, the cell potential would relax to 0 V vs. Li^+/Li once lithium is present on both electrodes, establishing a symmetric cell state, and would remain there indefinitely. In practice, if the electrolyte is unstable and side reactions occur, the deposited lithium is gradually consumed by these parasitic reactions. As long as some lithium metal remains at the WE, the potential is pinned at 0 V vs. Li^+/Li. Once the lithium is fully exhausted, the WE potential is no longer pinned and the cell voltage begins to rise, marking the end of the consumption period.

Stage I - Electrolyte Decomposition, Nucleation & Deposition

Each titration step begins with galvanostatic deposition, during which the potential is driven toward the lithium plating potential. Due to the low redox potential of lithium and the narrow thermodynamic stability window of LPSC, electrolyte decomposition and lithium nucleation are not strictly sequential. They can occur simultaneously, and the applied current can initially be sustained by interphase-forming reactions rather than lithium plating (see **Section 3.1**). This sequence is reflected in a characteristic nucleation overpotential peak in the voltage profile marked as V_{nuc} in Figure 4.6, the position and shape of which encodes information about both the interphase formation kinetics and the nucleation barrier, explained more in detail in **Section 3.1**.

Stage II - Lithium Consumption

Following deposition, the cell relaxes at OCV to approximately 0 V vs. Li^+/Li and chemically driven decomposition occurs (see Equations 3.1, 3.2-4). For LPSC, reduction and chemical reactions with lithium will produce a Li_2S, LiCl, and lithiated Li_xP containing interphase. This process establishes a lithium chemical potential gradient within the interphase, driving coupled Li^+ and e^- diffusion from the lithium front through the interphase to the solid electrolyte front [99].

The cell potential remains pinned at approximately 0 V vs. Li^+/Li as long as metallic lithium is present at the WE. Once the lithium is fully consumed, the potential begins to rise, marking the end of the consumption period. The duration of this consumption period is the central observable of the classic CTTA protocol [98] and scales with interphase thickness, since a thicker interphase presents a longer diffusion path. It is important to note, however, that the consumption time is sensitive not only to interphase thickness but also to its composition as it would modify the effective diffusivity through the percolation network where more highly lithiated Li_xP species have been reported to exhibit higher diffusivity than fully lithiated Li_3P [99].

In the classic protocol introduced by Aktekin et al. [98], a cut-off potential of 50 mV vs. Li^+/Li is used to define the end of each OCV period and the start of the next titration step.

Stage III - Delithiaiton

Burton et al. [99] revealed a process during full potential relaxation, beyond the 50 mV vs. Li^+/Li cut-off. Once metallic lithium is fully consumed, the boundary condition that pinned the chemical potential at the lithium front is lost. Li_3P

at the former inner interphase front is no longer in thermodynamic equilibrium with its surroundings and begins to spontaneously delithiate, progressing from Li_3P through partially lithiated Li_xP intermediates toward fully oxidized P^0. This manifests in a voltage plateau at approximately 0.87 V vs. Li^+/Li [125], corresponding to the $Li_3P \rightarrow Li_xP$ transition, before the potential stabilizes at a value close to the original OCV of the pristine cell.

The duration of the delithiation plateau was used in **Paper I** to evaluate the presence of Li_3P in the interphase, offering a potential compositional fingerprint that complements the thickness information encoded in the consumption time.

Using CTTA to Study Interphase Growth Kinetics

By applying successive titration steps, CTTA can track the evolution of the interphase over time. Figure 4.7a shows a single titration step, illustrating the deposition and subsequent consumption period during which the deposited lithium is progressively consumed by interfacial side reactions (see Fig. 4.6). At the second titration, the consumption time is visibly longer than in the first, as shown in Figure 4.7b, reflecting the growth of the interphase between the two steps. Across multiple successive titrations, Figure 4.7c, this progressive increase in consumption time becomes evident, providing a direct and qualitative measure of interphase growth with each cycle.

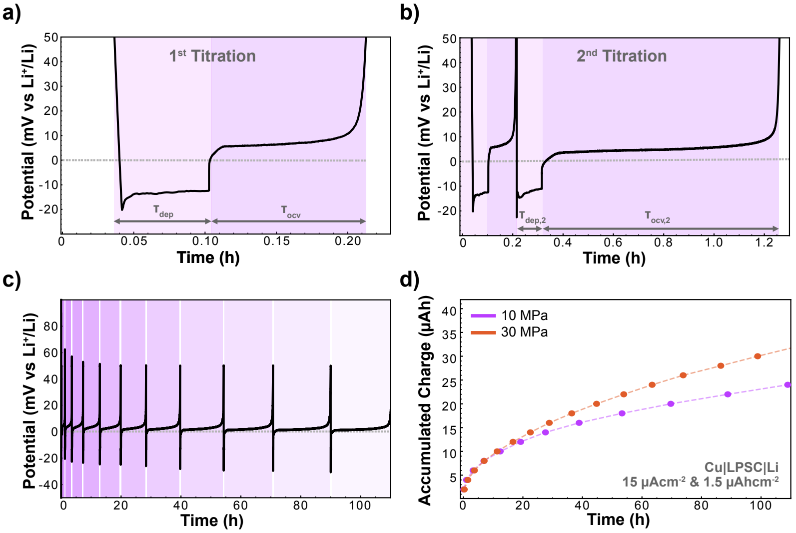

Figure 4.7: Coulometric titration time analysis of the lithium metal/LPSC/stainless steel cell. (a) Voltage profile of the first titration, showing the deposition of 1.5 μAhcm^{-2} at 15 μAcm^{-2} and following OCV consumption period. (b) Voltage profile showing the first and second titration. (c) Multiple successive titration. (d) Accumulated charge consumed by side reactions as a function of time for cells cycled at 10 MPa and 30 MPa stack pressure.

To quantify the growth kinetics, the accumulated charge consumed by side reactions can be tracked as a function of time, shown in Figure 4.7d. The square-root time dependence observed in the accumulated charge is consistent with diffusion-controlled growth as described by the Wagner model [60, 98, 99]. Whether and when growth slows or self-limits across successive titrations provides information about the passivating character of the formed interphase.

Figure 4.7d also illustrates how CTTA can be used to compare growth kinetics under different experimental conditions, here contrasting cells cycled at 10 MPa and 30 MPa stack pressure. The higher stack pressure results in faster lithium consumption, most likely due to improved interfacial contact providing more reaction sites [107] reinforcing the importance of stack pressure as a variable that must be carefully controlled and reported, as discussed in **Section 3.4** and **4.1**.

CTTA Protocol

The findings of Burton et al. [99] raise a practical question for CTTA protocol design and application. In the classic protocol, the OCV period is terminated at 50 mV vs. Li^+/Li (see. Fig. 4.8a), capturing only the consumption stage and excluding the delithiation of Li_3P.

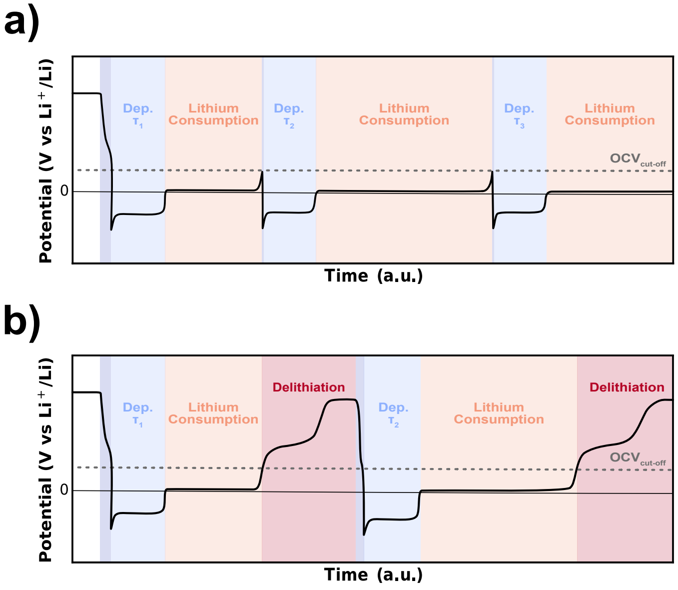

Figure 4.8: Schematic illustration of the CTTA protocols. a) CTTA measurement sequence introduced by Atkin et al. [98], consisting of repeated lithium deposition steps (blue regions) each followed by a voltage relaxation period (peach region) until the OCV reaches a cut-off potential of 50 mV vs. Li^+/Li before next lithium plating (titration) step. b) Modified version of the CTTA technique in which the OCV is allowed to relax beyond the voltage cut-off, incorporating a delithiation step [99] (red region) before the next titration.

In an alternative protocol, the cell is allowed to fully relax through the delithiation stage before initiating the next titration (see Fig. 4.8b). These two approaches leave the interphase in fundamentally different states at the start of the subsequent deposition, the classic protocol preserving a Li_3P-rich interphase. Since interphase diffusivity depends on the lithiation state of the phosphorus phases, the choice of protocol is expected to influence the consumption time. The implications of the choice of protocol and its effect on the observed interphase growth kinetics are investigated in **Paper I** and discussed further in **Chapter 6**.

Chapter 5

X-ray Characterization & Imaging of Interfaces

Understanding the processes occurring at the lithium metal/solid-state electrolyte interface requires characterization methods that can resolve both the chemical and morphological properties across a range of length scales, from the nanometre-thick interphase layers discussed in **Chapter 3** to the microscopic morphological changes associated with void formation, cracking, and dendrite propagation. As discussed in **Chapter 4**, electrochemical methods provide valuable but inherently indirect and spatially averaged information about these processes.

X-ray based methods offer a compelling alternative for characterizing buried interfaces. X-rays techniques enables non-destructive imaging without the need for cell disassembly making *in situ* and *operando* measurements possible. The contrast in X-ray imaging arises from how X-rays interact with matter, through absorption, refraction, scattering, and diffraction [126], and each of these interactions can be exploited to extract different types of material information.

This chapter introduces the physical principles underlying these interactions and the imaging modalities used in this thesis, X-ray attenuation-based micro-computed tomography (μCT), X-ray computed nano-holo-tomography (nanoCT), and X-ray diffraction computed tomography (XRD-CT), each exploiting a different contrast mechanism to provide complementary structural and chemical insight into the lithium/LPSC interface.

5.1 X-ray Interaction with Matter

X-rays are electromagnetic radiation with wavelengths ranging between approximately 0.01–10 nm, corresponding to photon energies in the range 100 keV to 100 eV [126]. In this thesis, X-ray photons in the range of 30–35 keV are used and their interactions with matter form the basis of the imaging techniques employed.

When an X-ray beam passes through a material (Fig. 5.1), it is modified in both amplitude and phase. These modifications can be described by the complex refractive index of the material,

$$n = 1 - \delta + i\beta \tag{5.1}$$

where the imaginary part β describes how the X-ray changes in amplitude when passing though the material [127]. β is related to the attenuation coefficient μ

through the relationship $\mu = 4\pi\beta/\lambda$, where λ is the X-ray wavelength. The real part of the refractive index $(1-\delta)$ describes the change in wavelength of the X-ray as it propagates though the material. A difference in the decrement, δ, between two materials lead to a phase shift of the X-rays. Materials have different β-values, leading to variations in the transmitted X-ray amplitude as a function of material composition and thickness. Likewise, the real part of the refractive index $(1-\delta)$ is also material dependent, and X-rays passing though a sample will acquire a path-dependent phase shift.

At the energies used in this thesis, δ is typically several orders of magnitude larger than β for light elements such as lithium, meaning that phase contrast is considerably stronger than absorption contrast [127]. The differences in attenuation- and phase-contrast is discussed further below in order to understand how and when the different mechanisms can be used for X-ray imaging.

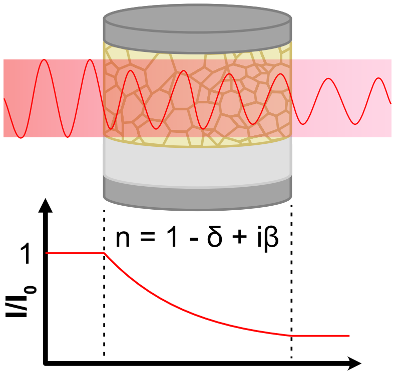

Figure 5.1: The transmission of X-rays through a material where attenuation causes a decrease in beam intensity, and refraction causes a deflection of the beam.

Attenuation Contrast

The attenuation of an X-ray beam as it passes through a material is described by Beer-Lambert's law,

$$I = I_0 e^{-\mu t} \tag{5.2}$$

where I_0 is the incident intensity, I is the transmitted intensity, t is the thickness of the material and μ is the linear attenuation coefficient [127]. The attenuation strongly depend on the atomic number Z, $(\mu \propto Z^3)$, and the density of the material, with heavier and denser materials attenuating more strongly. The attenuation is also dependent on the X-ray energy, E, and increases at lower energies $(\mu \propto E^{-4})$. This is the basis of conventional X-ray absorption-contrast imaging, where regions of different composition or density produce different levels of transmitted intensity, generating contrast in the image. Typically, to collect images with good enough X-ray attenuation contrast, the transmission should be around 14 % (I/I_0) [127]. To reach the targeted contrast can the beam energy E, or the sample thickness t be adjusted.

Phase Contrast
Although both the amplitude and phase of the transmitted wave are modified by the material (see Equation 5.1), detectors measure only intensity [126], which means that the phase information, encoded in δ, is not directly accessible from a single intensity measurement. However, phase information can be recovered by exploiting the interference properties of X-rays [127]. As a (partially) coherent beam propagates away from the sample, wavefronts that have been phase-shifted by different parts of the sample begin to interfere. The information on the phase shift is then contained within these fringes [128]. Phase retrieval is the process of extracting this phase shift. For phase contrast imaging, the image contrast is hence independent of μ, and so it is also independent of the transmission. Both δ and β are proportional to the electronic density of the material, but the decrement δ is independent on the atomic number [127]. This provides substantially enhanced contrast compared to pure attenuation imaging for light elements such as lithium. However, as the mapping of δ relies on the measurement of interference effects, a spatially coherent X-ray source is required [127]. Fourth generation synchrotron sources provides greatly increased spatial coherence compared to other X-ray sources, making phase retrieval possible [129, 130].

X-ray Diffraction
In addition to attenuation and phase effects, X-rays can interact with the periodic atomic structure of crystalline materials through coherent elastic scattering, forming the basis of X-ray diffraction (XRD) [126]. In most directions, the scattered X-rays interfere destructively, but in specific directions determined by the atomic arrangement, they interfere constructively, producing diffraction peaks. The condition for constructive interference is given by Bragg's law,

$$n\lambda = 2d \sin\theta \tag{5.3}$$

where λ is the X-ray wavelength, d is the spacing between crystallographic planes, θ is the angle between the planes and the incident beam, and n is the order of diffraction [126]. This relationship links the angles at which diffraction peaks occur to the crystal structure of the material. As a result, XRD provides direct information about lattice parameters, crystal phases, and structural ordering.

In transmission geometry, the incident X-ray beam passes through the sample and the diffracted intensity is collected over a range of angles, typically using a two-dimensional detector. The scattering is commonly described by the scattering vector Q, defined as,

$$Q = \frac{4\pi}{\lambda} \sin\theta \tag{5.4}$$

which provides a link between reciprocal space and real-space length scales [126].

For a powder sample, consisting of many randomly oriented crystallites, all possible diffraction conditions are satisfied, resulting in concentric rings (Debye rings) on the detector rather than discrete spots. Each ring corresponds to a specific scattering vector Q, and thus to a particular set of lattice spacings [126].

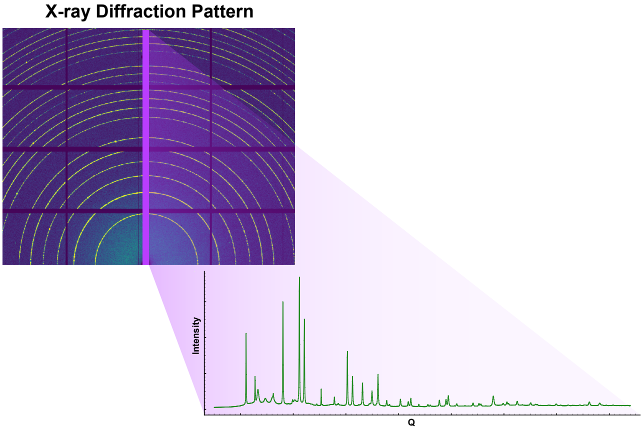

Figure 5.2: Azimuthal integration of the recorded 2D diffraction pattern to obtain a 1D diffraction pattern.

To obtain a one-dimensional diffraction pattern, the recorded two-dimensional intensity is typically azimuthally integrated (see Fig. 5.2). The resulting one-dimensional diffraction pattern can be used to identify the different crystalline phases based on the position of diffraction peaks. Other quantitative analysis can be made based on peak position shift, height, width or broadening.

5.2 Computed Tomography

With the fundamentals of X-ray-matter interactions and the resulting contrast mechanisms established, the remaining question is how to recover the three-dimensional information about the sample. Computed tomography (CT) provides the mathematical and experimental framework to achieve this. CT enables two- or three-dimensional reconstruction by collecting multiple images, projections, acquired from different angles. Each projection represents the line integral of the sample contribution along the X-ray beam path, such as attenuation, phase shift, or scattering intensity. This mathematical description corresponds to the Radon transform. [126]

By acquiring projections over multiple rotation angles, the data can be arranged into a sinogram, which represents the angular variation of the projected signal. The original three-dimensional structure is then reconstructed from the sinogram by applying a tomographic reconstruction algorithm, most commonly through filtered back-projection. This reconstruction principle (see Fig. 5.3) is independent of the specific contrast mechanism used and can be applied to absorption-, phase-contrast-, and scattering-based tomography, but certain contrast-specific steps needs to be added in the pipeline, such as phase retrieval for phase-contrast-based tomography for example. [126]

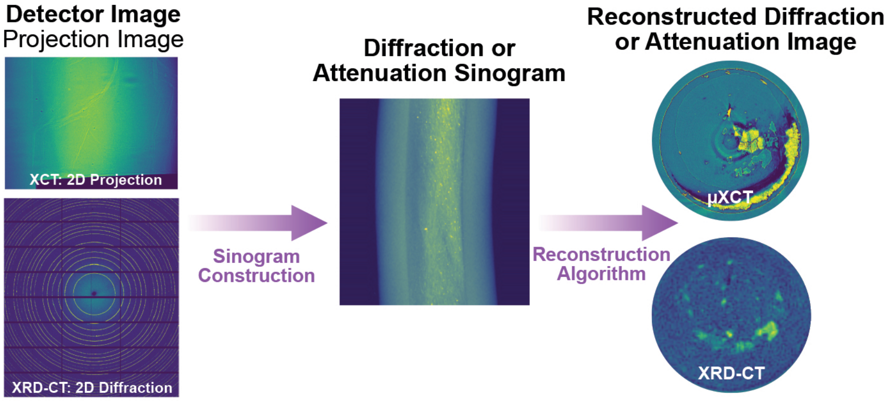

Figure 5.3: X-ray attenuation-based or X-ray diffraction-based data acquisition and reconstruction.

In phase-contrast tomography, additional phase retrieval methods are required to recover quantitative phase information prior to reconstruction. In this work, full phase retrieval is performed by acquiring data at multiple sample-to-detector distances (so-called holo-tomography). This multi-distance approach enables reconstruction of phase variations over a broader range of spatial frequencies. [128]

The choice of imaging technique plays a critical role in determining which features and processes that can be resolved, as each method relies on different contrast mechanisms and offers different spatial resolutions. This is illustrated in Figure 5.4, where complementary techniques are compared across length scales. As a comparison, optical microscopy provides an overview of the sample surface at the laboratory scale, enabling the observation of macroscopic features in the range of hundred-fold magnification. Absorption-based micro-computed tomography offers higher spatial resolution, typically in the range of a few micrometers [37], allowing visualization of features such as pellet density, cracking, and particle size distributions. Nano-scale or more specifically holotomography offers further improved spatial resolution down to 150 nm [131, 132], enabling the resolution of fine structural details such as fractures within individual solid electrolyte particles and increased contrast for low attenuating materials. X-ray diffraction computed tomography (XRD-CT) provides crystallographic information rather than purely structural contrast. It enables identification of phase distributions and chemical heterogeneities within the sample and the spatial resolution is limited by the beam size, which using synchrotrons can be made small whilst still having a high photon flux [129]. Together, these techniques provide complementary insights, and the appropriate choice depends on the specific length scale and type of information required.

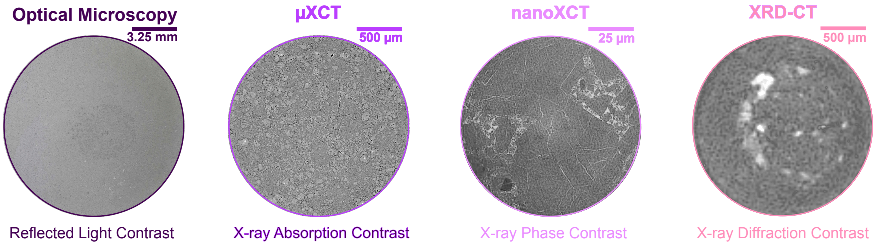

Figure 5.4: Horizontal cross-section of a solid-state battery cell imaged using, optical microscopy, X-ray computed micro-tomography, X-ray computed nano-holotomography, and X-ray diffraction computed tomography.

5.2.1 Image Analysis

Following reconstruction, a series of image processing steps are applied to extract quantitative and qualitative information from the tomographic data. While the specific parameters vary between datasets, the general workflow consists of pre-processing, segmentation, and (two- or) three-dimensional analysis.

Pre-processing
The reconstructed volume is first filtered to reduce noise to simplify the segmentation step. A median filter is commonly used, as it suppresses noise without significantly blurring edges, which is important to preserve interfaces [133]. The volume of interest is then selected by cropping, and the data may be binned or converted to lower bit depth to reduce computational cost.

Segmentation
Segmentation assigns each voxel in a volume, or pixel in an image, to a specific material or phase. When contrast is high (well-separated peaks in the gray-scale intensity histogram), simple thresholding based on the histogram can be sufficient to separate phases. An example is seen in Figure 5.5 where solid-electrolyte particles appear gray and cracks or porosities appear as black. The cracks and pores for example, can easily be segmented by labelling all voxels above a certain threshold as solid-state electrolyte, and all below as voids. However, in the presence of noise, artifacts, or sometimes complex multiphase structures, thresholding becomes unreliable. In such cases, as in the case for all work presented in this thesis, a machine learning-based tool called Ilastik can be employed [134], where a classifier is trained on manually labelled regions to segment the full dataset based on both intensity and local texture features.

3D analysis & visualization
Segmentation of a volume enables both visualization and quantitative analysis to be performed. Three-dimensional rendering in Paraview was used to inspect the spatial distribution of features [135]. Quantitative descriptors such as volume

fraction, surface area, and size distributions can then extracted, typically using custom python analysis scripts or Fiji ImageJ [136].

For diffraction-based tomography, analysis was done by generating phase distribution maps from the diffraction intensity integrated over a determined Q-range in Plaid [137]. Each pixel contains a local diffraction pattern, enabling phase identification. In such cases, reference patterns derived from crystallographic information files (CIFs), obtained from databases such as the Inorganic Crystal Structure Database (ICSD) [35], can be used for peak assignment and phase identification.

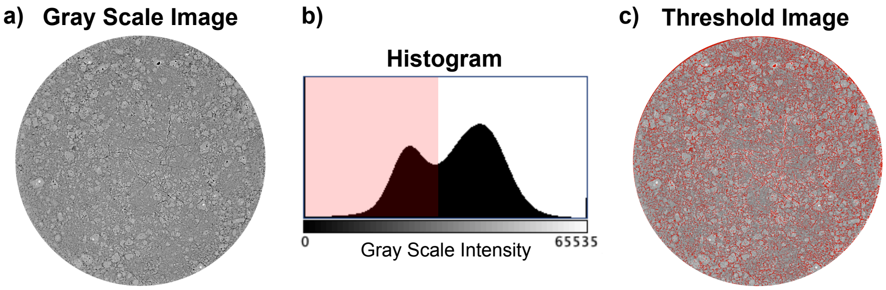

Figure 5.5: Segmentation using thresholding. a) A greyscale image showing a cross-sectional slice through a reconstructed tomogram showing gray solid-state electrolyte particles and black cracks and pores. b) Histogram of the greyscale values in a), the red region corresponds to values below a threshold. c) Pixels below the threshold marked in red.

Artifacts

Tomographic reconstructions are susceptible to a range of artifacts [127]. Ring artifacts are a frequent feature that manifests as concentric rings centred on the rotation axis. They typically arise from defective detector pixels, but can typically be removed using stripe removal of the sinogram during reconstruction. Moreover, inaccuracies in determining the centre of rotation can also result in circular or arc-shaped artifacts. Insufficient angular sampling leads to undersampling artifacts, often observed as star-like streaks that are more pronounced near the edges of the reconstruction. To minimize such effects, the number of projections should be proportional to the largest diameter of the sample in units of pixels [127]. In this work, approximately 2500-4500 projections are used, depending on the imaging modality. One common artifact in phase-sensitive imaging is edge enhancement, which originates from material-dependent refraction of partially coherent X-rays. This leads to bright-dark fringes at interfaces between different materials, enhancing edges and potentially complicating quantitative interpretation. Lastly, if the sample is larger than the field of view, and especially if high-density features are outside it, they can project into the scan region causing shadowing or streaking. This can be an artifact when performing local-tomography such as when the field of view is kept small to do high resolution imaging like nano-tomography.

5.2.2 Tomography Cell Design

For all X-ray experiments in this thesis, a dedicated electrochemical cell (Fig. 5.6) was used, designed by J. Rizell based on previous work by Sadd et al. [78] and inspired by [110]. The design is governed by several key considerations: (i) geometric constraints and compatibility with the beamline, (ii) X-ray transparency, and (iii) electrochemical functionality.

The cell geometry is optimized to match the field of view of the imaging setup, with an inner diameters of 2 mm. While smaller samples are generally preferred to maximize X-ray transmission [127], it is often impractical to build such a small cell. The housing of the cell is fabricated from polyether ether ketone (PEEK), a polymer with relatively low X-ray attenuation. In addition, PEEK exhibits good chemical stability against reactive components such as lithium metal. Moreover, its mechanical rigidity allows thin walls. O-ring seals ensure that the cell is airtight, and a spring-loaded mechanism enables controlled stack pressures in the range of 10^2 - 10^6 Pa.

The cell is designed to be compatible with beamline requirements, permitting stable mounting, rotation during acquisition, and *operando* electrical measurements. While PEEK is well suited for absorption- and phase-contrast tomography, it is crystalline and diffraction features can contribute to background scattering, making it less optimal for diffraction-based measurements.

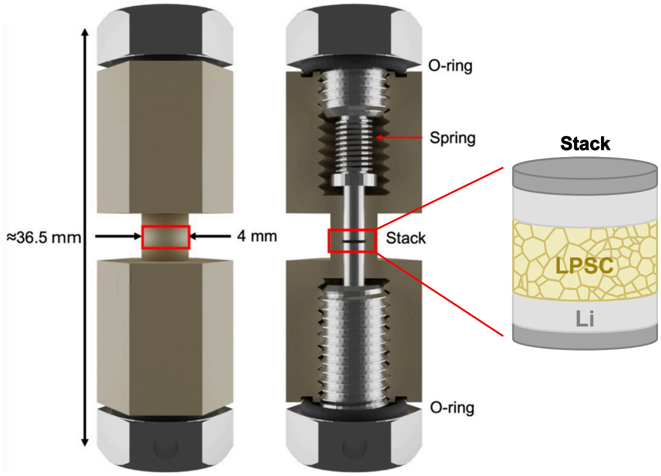

Figure 5.6: Three-dimensional illustration of the tomography cell and cross-section.

Chapter 6

Results - Chemical & Electrochemical Interphase Formation

In this chapter, the results of the appended papers are presented and discussed with the aim of understanding how the Li/LPSC interphase forms, evolves, and remains electrochemically active. We first establish the electrochemical indication of interfacial instability, before visualising the interfacial evolution. By combining these perspectives, a coherent picture of the Li/LPSC interface emerges, not as a uniform interphase layer, but as an evolving interphase whose structure, chemistry, and electrochemical behaviour are intrinsically linked.

6.1 Interfacial Instability

Thermodynamically, the lithium metal/LPSC interface is expected to be unstable. First-principle calculations predict that LPSC has a limited electrochemical stability window and is energetically driven to decompose to form Li_2S, LiCl, and lithiated phosphorus in contact with lithium metal, even in the absence of an applied current [22]. Coulometric titration time analysis (CTTA) provides a measure for such interfacial instability (**Section 4.4**, [98]). In an anode-free cell configuration, lithium metal is initially only present at the counter electrode, and the open-circuit potential will be approximately 1.7-1.9 V vs. Li^+/Li. Following the deposition of a small amount of lithium on the working electrode, the cell potential will relax toward 0 vs. Li^+/Li, as a result of the presence of lithium at both electrodes. In the ideal thermodynamically stable case, this state would remain stationary. Therefore, will any deviation from this reflect (electro)chemically driven interfacial reactions consuming the deposited lithium.

Figure 6.1a shows the voltage response following deposition of 15 μAhcm^{-2} of lithium at a current of 15 μAcm^{-2}. After deposition, the potential relaxes near 0 V vs. Li^+/Li for an extended period, approximately 39 hours, before rising abruptly. This voltage increase marks the complete consumption of the deposited lithium at the Li/LPSC interface even under open-circuit conditions. The finite duration of the consumption period demonstrates that the interface is unstable and that an interphase forms and evolves continuously until all lithium is depleted.

To further investigate the nature of this instability, electrochemical impedance spectroscopy was performed throughout the lithium consumption period. As shown in Figure 6.1b-c, the impedance response evolves with time, indicating a continuous evolution of the interface as lithium is being consumed. According to Burton et al. [99], interphase growth during the consumption stage is sustained by a chemical potential gradient across the interphase with coupled Li^+ and e^- transport through a percolating network of lithiated phosphorous species Li_xP and fully reduced Li_3P. Diffusion through the Li_xP path defines the rate-determining step for interphase growth, and its effective diffusivity depends on the lithiation state of the phosphorous species. In Figure 6.1b-c we see the evolution of the Nyquist and Bode plots. In particular, the response of the impedance and phase angle in the middle frequency regime (1 Hz to 10 kHz) increases in magnitude and shifts towards lower frequencies, potentially consistent with such transport-limited growth through a chemically evolving interphase.

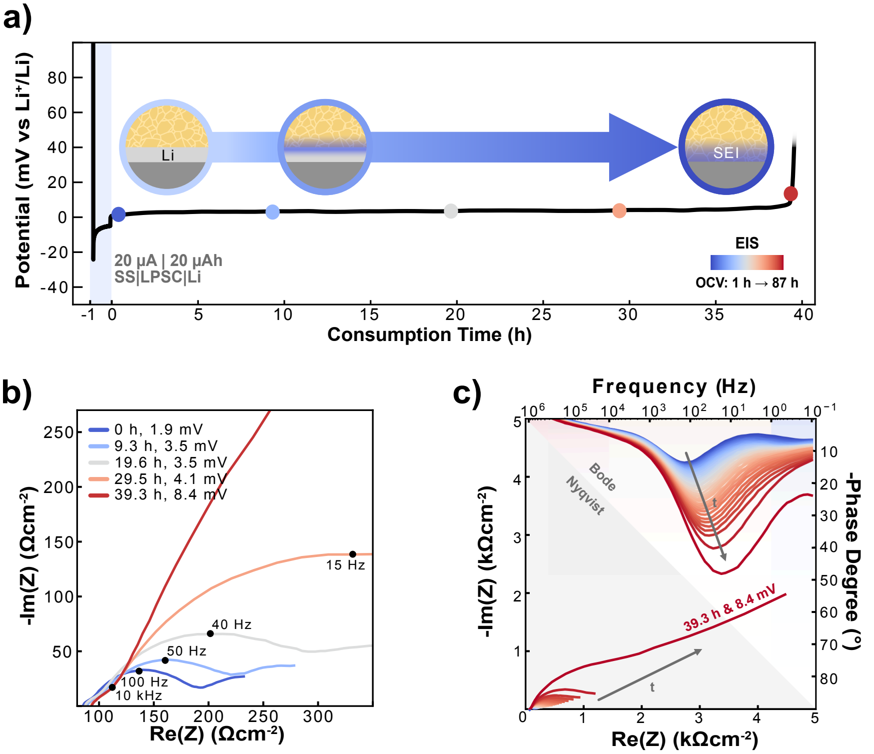

Figure 6.1: Interfacial instability between lithium and LPSC. a) Voltage response following deposition of 15 μAhcm^{-2} (20 μAh) of lithium at a current of 15 μAcm^{-2} (20 μA). The potential remains close to 0 V vs. Li^+/Li for 39.3 h starting from the end of deposition (-1 to 0 for 1 h). b) Nyquist plots acquired at selective time point during the lithium consumption period. c) Corresponding Nyquist and Bode plots during the entire time sequence.

As the cell voltage begins to deviate from 0 V vs. Li^+/Li, a diffusive low-frequency tail emerges in the impedance response, reflecting the transition towards an ion-blocking interface once all metallic lithium is exhausted at the working electrode. Importantly, a high-frequency semicircle persists even after full consumption (see Fig. 6.1b, 39.3 h at 8.4 mV), indicating the continued presence of a formed interphase at the current collector/LPSC interface. Together, these observations demonstrate that interphase formation proceeds continuously in contact with lithium metal.

6.2 Interphase Evolution

While electrochemical measurement can establish that the Li/LPSC interface is unstable and undergoes transport-limited interphase growth, they do not reveal where this interphase forms or how it evolves spatially. To address these questions, *operando* and *in situ* X-ray computed micro-tomography (μCT) was employed in **Paper II** to directly observe the Li/LPSC interface during cycling and stripping.

In Figure 6.2b, the voltage profile during cycling of a symmetric Li/LPSC/Li cell can be seen to polarize. This increase in overpotenial could indicate the formation of voids causing loss of contact or formation of a resistive interphase at the Li/LPSC interface (see **Chapter 3** for interfacial processes expected to occur at the Li/LPSC interface). To follow the interfacial evolution during cycling and to link the electrochemical signature to potential morphological changes, *operando* μCT was performed. The working electrode (Fig. 6.2a) was scanned continuously during cycling (Fig. 6.2b) and Figure 6.2c shows the cross-sections of the Li/LPSC interface acquired after.

In the pristine state, and throughout the first full cycle, no structural changes are observed at the interface beyond the volumetric changes associated with lithium plating and stripping. After the second plating however, a new phase appears locally at the Li/LSPC interface. The observed phase exhibits intermediate X-ray attenuation relative to that of lithium metal and the LPSC electrolyte, consistent with the potential formation of an interphase due to (electro)chemical degradation which would cause a chemically distinct region at the interface. Notably, this phase forms only locally at the interface, and is seen to grow downwards into the lithium metal rather than propagating up into the solid electrolyte. This local and directional growth into the lithium metal contrasts with the commonly used model of a laterally *uniform* interphase layer forming over the electrode [13, 55, 110].

The local formation could point towards an electrochemical reaction rather than a pure chemical reaction. Insufficient contact, contaminations, grain boundaries, surface defects, or flaws can all cause current hotspots at the Li/LPSC interface [13]. However, the newly formed phase continuous to grow during subsequent cycling, and importantly, during both plating and stripping. The growth and formation of new locally forming phases during both lithium deposition and stripping questions the attribution to simply reduction or oxidation. The local rather than uniform formation of the phase may be understood in terms of the spatial heterogeneity of the electrochemical potential at the Li/LPSC interface.

While the bulk thermodynamic driving force for LPSC to decompose against lithium metal is uniform, the real potential at the interface includes a surface potential contribution that will vary locally with the surface structure, defects, and contact meaning that surface heterogeneities could preferentially lower the nucleation barrier for decomposition, driving interphase formation at specific sites rather than uniformly across the contact area [97]. This points toward a more complex, coupled electro-chemical process.

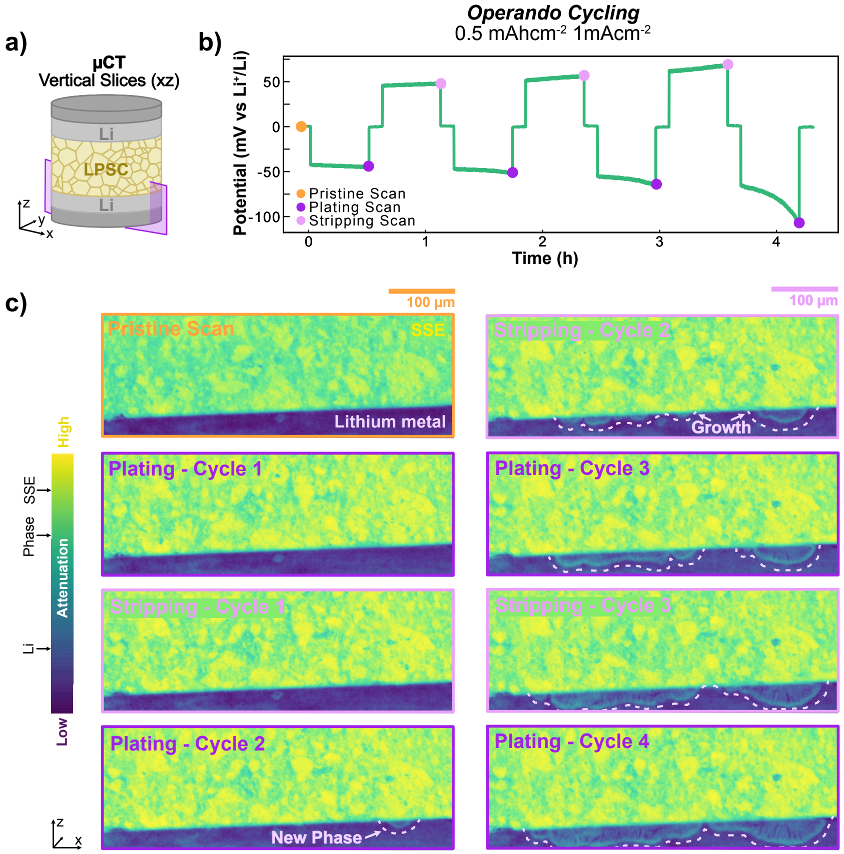

Figure 6.2: *Operando* μCT of the Li/LPSC interface during cycling. a) Schematic illustration of the symmetric Li/LPSC/Li cell and the position of the extracted slices though the working electrode. b) Voltage profile during cycling (0.5 mAhcm^{-2}, 1 mAcm^{-2}), with markers indication at which points the tomograms presented in c) was taken. c) Vertical cross-section through the Li/LPSC interface in the pristine cell and after each successive plating and stripping half-cycle demonstrating the localized interphase formation and growth.

To further isolate the nature of this growth a dedicated *in situ* μCT experiment was performed during stripping (**Paper II**). After 4.76 mAhcm^{-2} of stripped lithium, the same locally forming phase appears growing down into the lithium metal. Quantitive volume analysis allowed the lithium consumed associated with the formation of the phase to be distinguished from the lithium removed during electrochemical stripping. By segmentation of the lithium electrode before and after stripping, excluding the voxels containing the newly formed phase, the volume difference before and after could be calculated to a corresponding removal of 4.74 mAhcm^{-2} lithium, agreeing closely with the electrochemically measured stripped capacity. Whilst, the segmented phase volume corresponded to an additional removal of 0.27 mAhcm^{-2}lithium, suggesting that the volume of lithium removed to form the phase happened in addition to the volume removed during stripping. Assuming the density of lithium metal, 0.27 mAhcm^{-2} would correspond to a 1.3 μm homogenous layer if that the phase was assumed to form a uniform interphase across the entire interface. This is still thicker than the estimated thickness of a few hundreds of nanometers from CTTA [98] and ToF-SIMS [101]. However, important to note, the thickness calculations from [98, 101] is from a week of chemical degradation.

Together, these observations all highlight the complexity of this newly formed phase. To understand how such a locally forming, electrochemically active, phase can form and grow it is necessary to further investigate its internal structure and chemical heterogeneity.

6.3 Structural & Chemical Heterogeneity

6.3.1 Three-dimensional Multiphase Formation

High-resolution X-ray computed nano-tomography (nanoCT) was employed to resolve the internal structure of the phase formed at the Li/LPSC interface. A vertical nanoCT slice acquired after 8 mAhcm^{-2} of lithium stripping is shown in Figure 6.3b. A region at the interface, resembling that in Figure 6.2 with intermediate attenuation and non-uniform morphology is observed. Moreover, a clear heterogenous structure within the phase can be seen.

Segmentation of the formed phase reveals that the phase consist of at least two distinguishable components, one outer more attenuating phase surrounding a less attenuating inner phase (Fig. 6.3c). Moreover, the less attenuating phase (2nd phase), exhibits similar contrast to the surrounding lithium metal. Connectivity analysis of the inner less attenuating phase shows that the majority of the structure forms a single, interconnecting network, with only a minor fraction of isolated fragments as shown in Figure 6.3d. The mean local thickness of the inner phase was calculated to be approximately 769 nm, substantially smaller than the reported lithium metal foil grain size of 100-300 μm [81]. While the nanoCT contrast alone does not uniquely determine chemical composition, the observed connectivity and morphology are consistent with the presence of lithium-rich or lithium-containing species capable of supporting coupled ionic and electronic transport.

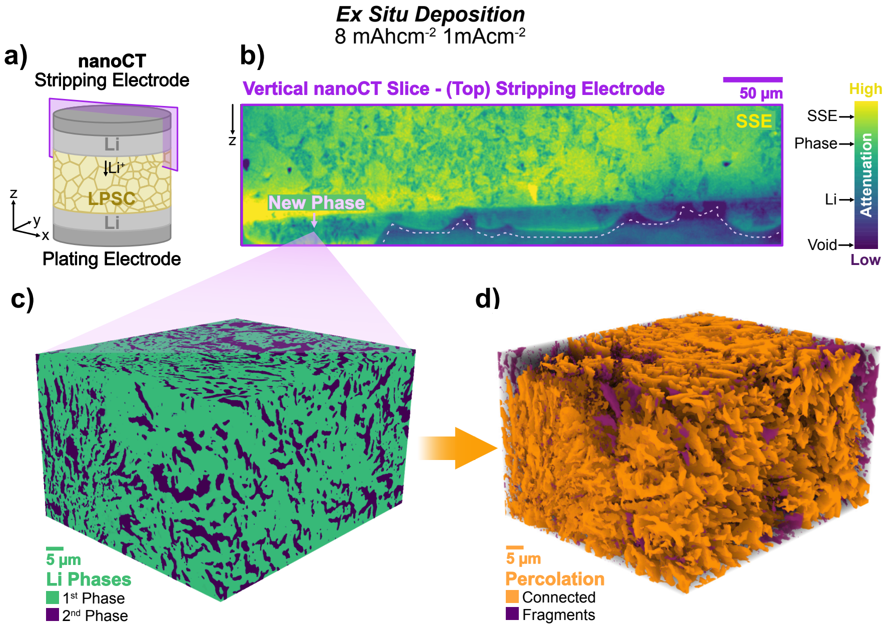

Figure 6.3: *Ex situ* nanoCT of the interface after stripping. a) Schematic illustration showing the position of the nanoCT scan at the stripping electrode. b) Vertical cross-section acquired after 8 mAhcm^{-2} of stripping revealing a structurally heterogenous phase formed at the Li/LPSC interface. c) Three-dimensional volume rendering of the segmented phase showing two distinguishable regions, an outer more attenuation phase (1st phase) and an inner less attenuating phase (2nd phase). d) Connectivity analysis of the inner, low-attenuation phase where orange indicates regions of connected structures and purple isolated fragments.

6.3.2 Electrochemical Signatures

While nanoCT reveals the morphology of the phase, in **Paper I** we asses the presence of electronically conductive species in the interphase by modifying the CTTA protocol. In particular, comparing a pristine cell and a cell subjected to an interphase pre-formation step prior to CTTA allows to probe, and asses the electrochemical signatures of interphase thickness and/or composition using a single titration step.

Figure 6.4a schematically illustrates the electrochemical stages during one full coulometric titration step when full voltage relaxation is allowed, highlighting electrolyte decomposition and nucleation, lithium deposition, lithium consumption, and delithiation of lithiated phosphorus species. Each step is explained more in detail in **Section 4.4**.

Comparing the voltage profiles of a cell without, and a cell with pre-formation (potentiostatic hold at 10 mV vs. Li$^+$/Li for 15 minutes) performed before galvanostatic deposition, we see a shift in the nucleation event during deposition in Figure 6.4b. For nucleation on a pristine substrate, nucleation occurred after approximately 65 seconds, whereas following the pre-formation, the nucleation delay is reduced to approximately 23 seconds. This shows that the pre-formation modifies the extent to which kinetically driven electrolyte decomposition competes with lithium nucleation. However, the fact that the nucleation delay remains substantial even after pre-formation indicates that the formed interphase does not provide complete passivation. Instead it suggests presence of electronically conductive interphase components, consistent with the formation a mixed-conducting interphase that is expected due to the incorporation of lithiated phosphorus.

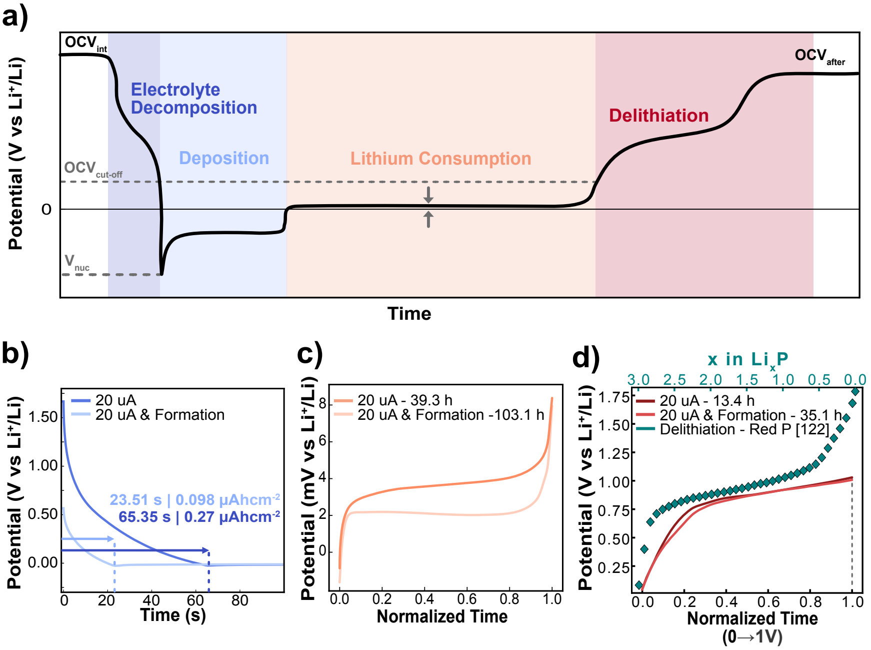

Figure 6.4: a) Schematic illustration of electrochemical stages during one extended coulometric titration step, (i) electrolyte decomposition and nucleation, (ii) lithium deposition, (iii) lithium consumption, (iv) and delithiation of lithiated phosphorus. Voltage profile comparing a pristine cell and a pre-formed cell (potentiostatic hold at 10 mV vs. Li^+/Li for 15 minutes) showing b) the nucleation and early deposition stage, c) the lithium consumption stage, and d) the delithation normalized to the time until reaching 1 V vs. Li^+/Li. The delithiation of red phosphorus from [125] is also included in d).

Following lithium deposition, the cells relax to an open-circuit potential near 0 V vs. Li^+/Li (Fig. 6.4c). Despite the same deposited capacity (15 $\mu Ahcm^{-2}$), the duration of the consumption stage differs markedly between the cell with and without pre-formation. In the cell without pre-formation, the deposited lithium is consumed within 39 hours, defined by the time the voltage abruptly starts to increase, whereas in the pre-formed cell, the consumption time is extended to 103 hours. Correction for differences in the effective deposited lithium arising from the nucleation delay shows that this effect accounts for only minutes of the total consumption time and cannot explain the observed differences. The variation in consumption time therefore reflects real differences in the properties of the interphase at the onset of consumption rather than differences in the amount of metallic lithium available.

According to the framework proposed by Burton et al. [99], lithium consumption during this stage is governed by diffusion through a percolating network of lithiated phosphorus species within the interphase. The effective diffusivity of this network is not constant but depends on the lithiation state of the phosphorus phases. The observed differences in consumption time are thus consistent with differences in interphase thickness or degree of lithiation, both of which modify the effective transport resistance through the interphase.

Once metallic lithium is fully exhausted, the cell potential rises and a distinct delithiation stage is observed (Fig. 6.4d). As described by Burton et al. [99], this potential rise reflects an active chemical transformation within the interphase. Removal of the metallic lithium eliminates the boundary condition that pined the lithium chemical potential at the interphase inner front, now making lithium-rich interphase components thermodynamically unstable. As a result, lithium-rich phosphorus species begin to delithiate, progressing from Li_3P toward partially lithiated Li_xP species, giving rise to a characteristic voltage plateau at approximately 0.87 V vs. Li^+/Li. In Figure 6.4d, the delithiation profile is normalized to the point it reaches 1 V vs. Li^+/Li, just after the plateau that mirrors the delithation of red phosphorus [125].

The duration of this delithiation plateau varies systematically with interphase properties, extending from approximately 13 hours to 35 hours by doing a pre-formation indicating a larger reservoir of lithium-rich interphase species or a longer diffusion path through the interphase after pre-formation. Importantly, the plateau length does not provide a direct measure of Li_3P volume fraction. Instead, it reflects a convolution of interphase thickness, lithium-rich phase fraction, and the evolving transport properties during delithiation, as delithiation itself modifies the local diffusivity and electronic connectivity of the interphase and drives further electrolyte decomposition [99].

6.3.3 Phase Identification

To directly probe the chemical compositon of the interphase, X-ray diffraction computed tomography (XRD-CT) was performed at a depth position near the Li/LPSC interface following stripping of 4.76 $\mathrm{mAhcm^{-2}}$ of lithium. Figure 6.5b shows the integrated intensity map over a Q range 1.98-1.99 $\mathrm{Å^{-1}}$, where a few locally confined regions exhibit high intensity. These high intensity regions coincide with the local formation of the intermediate attenuation phase identified earlier in the *operando* μCT (Fig. 6.2c), *ex situ* nanoCT (Fig. 6.3b) now visible in the μCT horizontal slice close to the Li/LPSC interface in Figure

6.5c. While exact voxel-by-voxel overlap in Figure 6.5b-c cannot be expected due to the significantly larger effective slice thickness of XRD-CT (24μm) compared to μCT (550nm), the identical shape of the main feature confirms that the signal originates from the same spatially localized phase.

The XRD pattern extracted from a high-intensity pixel within the phase map, at a position confirmed by µCT to coincide with the formed phase, is shown in Figure 6.5d. Six peaks are identified in this pattern at $Q = 1.61, 1.985, 3.24, 3.44, 3.80$, and 4.73 Å^{-1}, marked in Figure 6.5d. The resulting phase map for each of these peaks co-localize to high intensity diffraction signal in same spatial region. Moreover, Figure 6.5d-g compares the XRD patterns extracted from the pixel inside the interphase region and a pixel outside it, containing only lithium metal and LPSC electrolyte, as illustrated schematically in Figure 6.5h. The six peaks identified in Figure 6.5d are present in the pattern from within the interphase and absent in the XRD pattern from outside, confirming that they arise specifically from the phase. Comparison of the two patterns also shows that the diffraction signal of LPSC (ICSD Collection Code 217792) and lithium metal (ICSD Collection Code 642104) are not substantially altered inside the phase relative to outside, suggesting that the bulk crystallographic structure of the surrounding electrolyte and lithium metal is not disrupted within the probed volume or at this scale. Importantly, no single crystalline phase provides a unique match to all observed peaks. Instead, the diffraction features are consistent with contributions from multiple phases, including S_8, Li_2S, and different crystal structures of lithium metal.

The structural and chemical heterogeneity support the picture of a chemically complex, multiphase interphase. The presence of lithium-like diffraction signatures within the phase could suggest that lithium metal or structurally related lithium-rich phases may be retained or enclosed within the interphase, consistent with the observation of a low-attenuating internal lamella like structure inside the phase, see Figure 6.3.

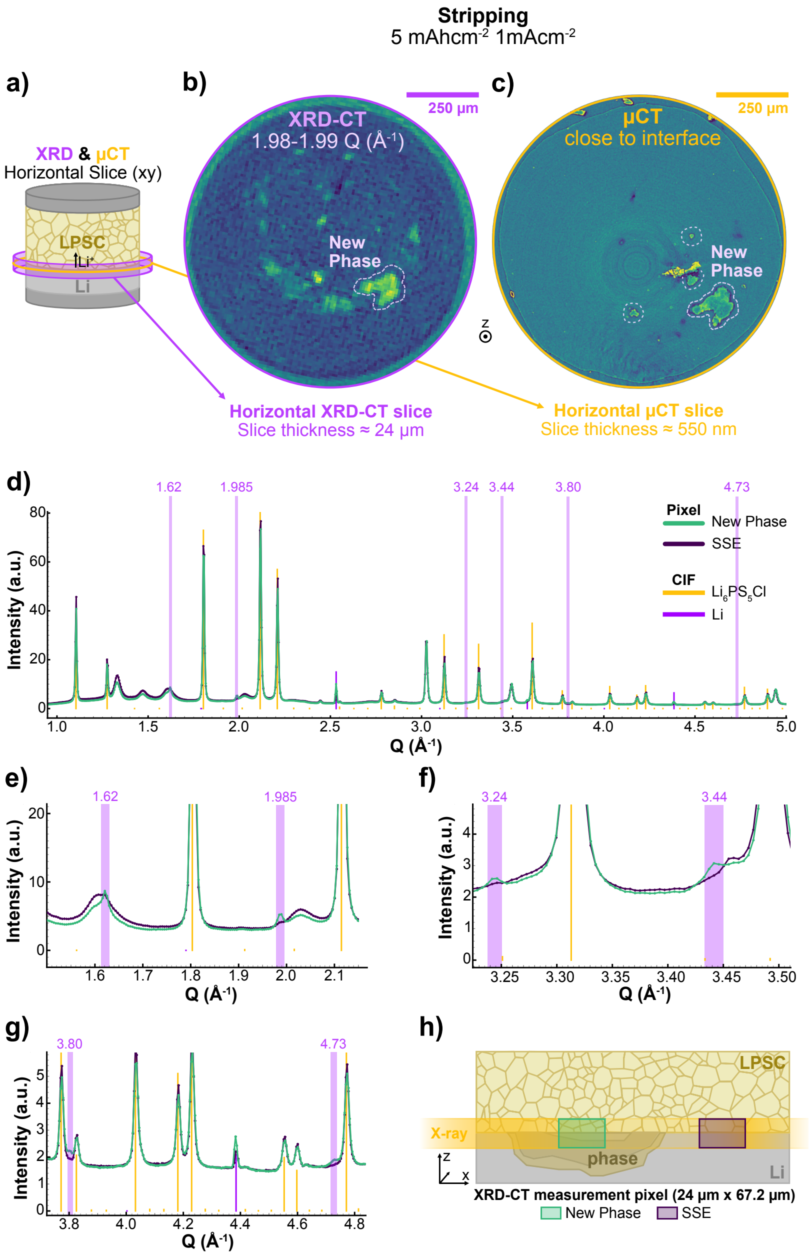

Figure 6.5: a) Schematic showing the position of the horizontal XRD-CT slice and corresponding μCT slice. b) XRD-CT integrated intensity map for Q=1.98–1.99 Å^{-1}. c) Horizontal μCT cross-section near the Li/SSE interface. d) XRD pattern extracted from pixels inside and outside the phase, with reference peaks for LPSC and Li. e–g) Zoomed comparisons of the phase specific peaks: e) 1.62 and 1.985 Å^{-1}, f) 3.24 and 3.44 Å^{-1}, and g) 3.80 and 4.73 Å^{-1}. h) Schematic illustrating the position of the extracted XRD-CT pixels.

Chapter 7

Conclusions & Outlook

The application of lithium metal as the anode material for solid-state batteries (SSBs) is often regarded as the *holy grail* due to its high gravimetric and volumetric energy density. At the same time, the use of lithium metal anodes is persistently challenged by interfacial instability. A central question raised in the introduction of this thesis was therefore whether solid-state electrolytes enable the use of lithium metal electrodes.

The results presented from **Paper I** and **II** demonstrate that the Li/LPSC interface remains unstable. The application of a modified coulometric titration time analysis experiment revealed continuous lithium consumption, even under open-circuit conditions, and electrochemical signatures that strongly depend on the electrochemical protocol and interfacial history. These observations may explain why different interphase thicknesses and growth kinetics have been reported across literature. Rather than reflecting inconsistencies, such discrepancies could arise from differences in applied current and interfacial state. At the same time, computed tomography revealed that interphase formation does not occur as a laterally uniform layer at the lithium/LPSC interface. Instead, the interphase was found to form locally at the interface and grow into the bulk lithium metal during both plating and stripping. High-resolution X-ray nano-computed tomography further demonstrated that the formed phase is structurally and chemically heterogeneous, consisting of distinctly different phases forming a connected sub-micron network.

Beyond the specific Li/LPSC system used in this thesis, these findings raise broader questions regarding how interphases in SSBs are conceptualized and modelled. While multiphase or multilayer interphases from a chemical composition standpoint have been proposed, solid-state interphases are still frequently treated as laterally uniform layers characterized primarily by their average thickness or chemical composition. In liquid-electrolyte systems, by contrast, extensive work has been done on the corresponding solid electrolyte interphase and its nanostructure, leading to mosaic, multilayer, or amorphous structural models [138]. The present work shows that solid-state interphases exhibit complex spatial organization, internal connectivity, and composition-dependent transport that cannot be captured by uniform growth models.

Future work should therefore focus on identifying the chemical nature and origin of the observed phase transformation using complementary characterization techniques, in order to obtain a more complete picture of the interphase formation process. Such investigations are necessary to assess whether the observed behaviour is unique to LPSC in contact with lithium metal, or if similar transformations may occur in other sulphide-based solid-state electrolytes or even in sodium-ion analogues for example. In parallel, future studies could explore interface-engineering strategies aimed at mitigating interfacial instability, for example through the introduction of interlayers or the use of alloying electrode materials, to evaluate whether the growth and evolution of such phases can be suppressed or controlled. Importantly. when looking forward, these results highlight the need to embrace the full structural and chemical complexity of solid-state interphases, only then can the prospects of stable alkali-metal electrodes be meaningfully assessed.

Bibliography

[1] K. Xu, *Electrolytes, Interfaces and Interphases. Fundamentals and Applications in Batteries.* Royal Society of Chemistry, 2023.

[2] J. B. Goodenough and K. S. Park, 'The Li-ion rechargeable battery: A perspective,' *Journal of the American Chemical Society*, vol. 135, no. 4, pp. 1167–1176, Jan. 2013, ISSN: 00027863. DOI: `10.1021/JA3091438/ASSET/IMAGES/JA-2012-091438{\_}M014.GIF`.

[3] M. Li, J. Lu, Z. Chen and K. Amine, '30 Years of Lithium-Ion Batteries,' *Advanced Materials*, vol. 30, no. 33, p. 1 800 561, Aug. 2018, ISSN: 1521-4095. DOI: `10.1002/ADMA.201800561`.

[4] J. Xie and Y. C. Lu, 'A retrospective on lithium-ion batteries,' *Nature Communications 2020 11:1*, vol. 11, no. 1, pp. 2499–, May 2020, ISSN: 2041-1723. DOI: `10.1038/s41467-020-16259-9`.

[5] W. Beard Kirby, *Linden's Handbook of Batteries*, 5th, McGraw-Hill Education, Ed. 2019.

[6] E. Peled, 'The Electrochemical Behavior of Alkali and Alkaline Earth Metals in Nonaqueous Battery Systems—The Solid Electrolyte Interphase Model,' *Journal of The Electrochemical Society*, vol. 126, no. 12, pp. 2047–2051, Dec. 1979, ISSN: 0013-4651. DOI: `10.1149/1.2128859/XML`.

[7] E. Peled and S. Menkin, 'Review—SEI: Past, Present and Future,' *Journal of The Electrochemical Society*, vol. 164, no. 7, A1703–A1719, Jun. 2017, ISSN: 0013-4651. DOI: `10.1149/2.1441707JES/XML`.

[8] D. Aurbach, B. Markovsky, A. Shechter, Y. Ein-Eli and H. Cohen, 'A Comparative Study of Synthetic Graphite and Li Electrodes in Electrolyte Solutions Based on Ethylene Carbonate-Dimethyl Carbonate Mixtures,' *Journal of The Electrochemical Society*, vol. 143, no. 12, pp. 3809–3820, Dec. 1996, ISSN: 0013-4651. DOI: `10.1149/1.1837300/XML`.

[9] J.-G. Zhang, W. Xu and W. A. Henderson, 'Lithium Metal Anodes and Rechargeable Lithium Metal Batteries,' Springer Series in Materials Science, vol. 249, 2017. DOI: `10.1007/978-3-319-44054-5`.

[10] J. Deng, C. Bae, A. Denlinger and T. Miller, 'Electric Vehicles Batteries: Requirements and Challenges,' *Joule*, vol. 4, no. 3, pp. 511–515, Mar. 2020, ISSN: 25424351. DOI: `10.1016/j.joule.2020.01.013`.

[11] B. Dunn, H. Kamath and J. M. Tarascon, 'Electrical energy storage for the grid: A battery of choices,' *Science*, vol. 334, no. 6058, pp. 928–935, Nov. 2011, ISSN: 10959203. DOI: `10.1126/SCIENCE.1212741/SUPPL{\_}FILE/DUNN-SOM.PDF`.

[12] H. Wang et al., 'Alkali Metal Anodes for Rechargeable Batteries,' *Chem*, vol. 5, no. 2, pp. 313–338, Feb. 2019, ISSN: 2451-9294. DOI: `10.1016/J.CHEMPR.2018.11.005`.

[13] T. Krauskopf, F. H. Richter, W. G. Zeier and J. Janek, 'Physicochemical Concepts of the Lithium Metal Anode in Solid-State Batteries,' *Chemical Reviews*, vol. 120, no. 15, pp. 7745–7794, Aug. 2020, ISSN: 15206890. DOI: `10.1021/ACS.CHEMREV.0C00431/ASSET/IMAGES/LARGE/CR0C00431{\_}0036.JPEG`.

[14] X. B. Cheng, R. Zhang, C. Z. Zhao and Q. Zhang, 'Toward Safe Lithium Metal Anode in Rechargeable Batteries: A Review,' *Chemical Reviews*, vol. 117, no. 15, pp. 10 403–10 473, Aug. 2017, ISSN: 15206890. DOI: `10.1021/ACS.CHEMREV.7B00115/ASSET/IMAGES/MEDIUM/CR-2017-00115D{\_}0044.GIF`.

[15] Q. Wu, E. D. Esping, M. Afiandika, S. Xiong and A. Matic, 'Understanding the electro-chemo-mechanics of lithium metal anodes,' *eScience*, vol. 6, no. 1, p. 100 429, Jan. 2026, ISSN: 2667-1417. DOI: `10.1016/J.ESCI.2025.100429`.

[16] J. Janek and W. G. Zeier, 'A solid future for battery development,' *Nature Energy 2016 1:9*, vol. 1, no. 9, pp. 16 141–, Sep. 2016, ISSN: 2058-7546. DOI: `10.1038/nenergy.2016.141`.

[17] C. Monroe and J. Newman, 'The Impact of Elastic Deformation on Deposition Kinetics at Lithium/Polymer Interfaces,' *Journal of The Electrochemical Society*, vol. 152, no. 2, A396, Jan. 2005, ISSN: 00134651. DOI: `10.1149/1.1850854/XML`.

[18] N. Kamaya et al., 'A lithium superionic conductor,' *Nature Materials 2011 10:9*, vol. 10, no. 9, pp. 682–686, Jul. 2011, ISSN: 1476-4660. DOI: `10.1038/nmat3066`.

[19] H. J. Deiseroth et al., 'Li6PS5X: A class of crystalline Li-rich solids with an unusually high Li+ mobility,' *Angewandte Chemie - International Edition*, vol. 47, no. 4, pp. 755–758, 2008, ISSN: 14337851. DOI: `10.1002/anie.200703900`.

[20] J. A. Lewis, J. Tippens, F. J. Q. Cortes and M. T. McDowell, 'Chemo-Mechanical Challenges in Solid-State Batteries,' *Trends in Chemistry*, vol. 1, no. 9, pp. 845–857, Dec. 2019, ISSN: 2589-7209. DOI: `10.1016/J.TRECHM.2019.06.013`.

[21] Q. Wu, S. Xiong, F. Li and A. Matic, 'Electro-Chemo-Mechanical Failure Mechanisms of Solid-State Electrolytes,' *Batteries & Supercaps*, vol. 6, no. 11, e202300321, Nov. 2023, ISSN: 2566-6223. DOI: `10.1002/BATT.202300321`.

[22] Y. Zhu, X. He and Y. Mo, 'Origin of Outstanding Stability in the Lithium Solid Electrolyte Materials: Insights from Thermodynamic Analyses Based on First-Principles Calculations,' *ACS Applied Materials and Interfaces*, vol. 7, no. 42, pp. 23 685–23 693, Oct. 2015, ISSN: 19448252. DOI: `10.1021/ACSAMI.5B07517/ASSET/IMAGES/LARGE/AM-2015-07517G{\_}0004.JPEG`.

[23] S. Wenzel, S. J. Sedlmaier, C. Dietrich, W. G. Zeier and J. Janek, 'Interfacial reactivity and interphase growth of argyrodite solid electrolytes at lithium metal electrodes,' *Solid State Ionics*, vol. 318, pp. 102–112, May 2018, ISSN: 0167-2738. DOI: `10.1016/J.SSI.2017.07.005`.

[24] L. M. Riegger, S. Mittelsdorf, T. Fuchs, R. Rueß, F. H. Richter and J. Janek, 'Evolution of the Interphase between Argyrodite-Based Solid Electrolytes and the Lithium Metal AnodeThe Kinetics of Solid Electrolyte Interphase Growth,' *Chemistry of Materials*, vol. 35, no. 13, pp. 5091–5099, Jul. 2023, ISSN: 15205002. DOI: `10.1021/ACS.CHEMMATER.3C00676/ASSET/IMAGES/LARGE/CM3C00676{\_}0005.JPEG`.

[25] M. Winter, B. Barnett and K. Xu, 'Before Li Ion Batteries,' *Chemical Reviews*, vol. 118, no. 23, pp. 11 433–11 456, Dec. 2018, ISSN: 15206890. DOI: `10.1021/ACS.CHEMREV.8B00422/ASSET/IMAGES/LARGE/CR-2018-00422Q{\_}0015.JPEG`.

[26] K. Schmidt-Rohr, 'How Batteries Store and Release Energy: Explaining Basic Electrochemistry,' *Journal of Chemical Education*, vol. 95, no. 10, pp. 1801–1810, Oct. 2018, ISSN: 19381328. DOI: `10.1021/ACS.JCHEMED.8B00479/ASSET/IMAGES/LARGE/ED-2018-00479Z{\_}0007.JPEG`.

[27] M. S. Whittingham, 'Ultimate limits to intercalation reactions for lithium batteries,' *Chemical Reviews*, vol. 114, no. 23, pp. 11 414–11 443, Dec. 2014, ISSN: 15206890. DOI: `10.1021/CR5003003/ASSET/IMAGES/LARGE/CR-2014-003003{\_}0044.JPEG`.

[28] J. Liu et al., 'Pathways for practical high-energy long-cycling lithium metal batteries,' *Nature Energy 2019 4:3*, vol. 4, no. 3, pp. 180–186, Feb. 2019, ISSN: 2058-7546. DOI: `10.1038/s41560-019-0338-x`.

[29] S. F. Lux, I. T. Lucas, E. Pollak, S. Passerini, M. Winter and R. Kostecki, 'The mechanism of HF formation in LiPF6 based organic carbonate electrolytes,' *Electrochemistry Communications*, vol. 14, no. 1, pp. 47–50, Jan. 2012, ISSN: 1388-2481. DOI: `10.1016/J.ELECOM.2011.10.026`.

[30] R. Fong, M. C. Reid, R. S. McMillan and J. R. Dahn, 'In Situ Study of Electrolyte Reactions in Secondary Lithium Cells,' *Journal of The Electrochemical Society*, vol. 134, no. 3, pp. 516–519, Mar. 1987, ISSN: 0013-4651. DOI: `10.1149/1.2100501/XML`.

[31] P. Zhou, X. Zhang, Y. Xiang and K. Liu, 'Strategies to enhance Li+ transference number in liquid electrolytes for better lithium batteries,' *Nano Research*, vol. 16, no. 6, pp. 8055–8071, Jun. 2023, ISSN: 19980000. DOI: `10.1007/S12274-022-4833-1/METRICS`.

[32] J. C. Bachman et al., ‘Inorganic Solid-State Electrolytes for Lithium Batteries: Mechanisms and Properties Governing Ion Conduction,’ *Chemical Reviews*, vol. 116, no. 1, pp. 140–162, Jan. 2016, ISSN: 15206890. DOI: `10.1021/ACS.CHEMREV.5B00563/ASSET/IMAGES/LARGE/CR-2015-005635{\_}0027.JPEG`.

[33] J. Huang et al., ‘Solid-State Electrolytes for Lithium Metal Batteries: State-of-the-Art and Perspectives,’ *Advanced Functional Materials*, vol. 35, no. 1, p. 2 411 171, Jan. 2025, ISSN: 1616-3028. DOI: `10.1002/ADFM.202411171`.

[34] Y. Kato, S. Shiotani, K. Morita, K. Suzuki, M. Hirayama and R. Kanno, ‘All-Solid-State Batteries with Thick Electrode Configurations,’ *Journal of Physical Chemistry Letters*, vol. 9, no. 3, pp. 607–613, Feb. 2018, ISSN: 19487185. DOI: `10.1021/ACS.JPCLETT.7B02880/ASSET/IMAGES/LARGE/JZ-2017-02880Z{\_}0004.JPEG`.

[35] J. W. Fergus, ‘Recent developments in cathode materials for lithium ion batteries,’ *Journal of Power Sources*, vol. 195, no. 4, pp. 939–954, Feb. 2010, ISSN: 0378-7753. DOI: `10.1016/J.JPOWSOUR.2009.08.089`.

[36] N. Boaretto et al., ‘Lithium solid-state batteries: State-of-the-art and challenges for materials, interfaces and processing,’ *Journal of Power Sources*, vol. 502, p. 229 919, Aug. 2021, ISSN: 0378-7753. DOI: `10.1016/J.JPOWSOUR.2021.229919`.

[37] E. P. Alsaç et al., ‘Characterizing Electrode Materials and Interfaces in Solid-State Batteries,’ *Chemical Reviews*, vol. 125, no. 4, pp. 2009–2119, Feb. 2025, ISSN: 15206890. DOI: `10.1021/ACS.CHEMREV.4C00584/ASSET/IMAGES/LARGE/CR4C00584{\_}0047.JPEG`.

[38] T. Schmaltz, T. Wicke, L. Weymann, P. Voß, C. Neef and A. Thielmann, ‘Solid-State Battery Roadmap 2035+,’ 2022. DOI: `10.24406/PUBLICA-68`.

[39] H. Huo and J. Janek, ‘Solid-state batteries: from ‘all-solid’ to ‘almost-solid’,’ *National Science Review*, vol. 10, no. 6, May 2023, ISSN: 2095-5138. DOI: `10.1093/NSR/NWAD098`.

[40] F. Strauss et al., ‘2026 Roadmap on Next-Generation Solid Electrolytes for Battery Applications,’ *Materials Futures*, Mar. 2026, ISSN: 2752-5724. DOI: `10.1088/2752-5724/AE5120`.

[41] J. Mindemark, M. J. Lacey, T. Bowden and D. Brandell, ‘Beyond PEO—Alternative host materials for Li+-conducting solid polymer electrolytes,’ *Progress in Polymer Science*, vol. 81, pp. 114–143, Jun. 2018, ISSN: 0079-6700. DOI: `10.1016/J.PROGPOLYMSCI.2017.12.004`.

[42] H. Gudla, K. Edström and C. Zhang, ‘Salt Effects on the Mechanical Properties of Ionic Conductive Polymer: A Molecular Dynamics Study,’ *ACS Materials Au*, vol. 4, no. 3, pp. 300–307, May 2024, ISSN: 26942461. DOI: `10.1021/ACSMATERIALSAU.3C00098/ASSET/IMAGES/LARGE/MG3C00098{\_}0007.JPEG`.

[43] S. Huo et al., 'Challenges of polymer electrolyte with wide electrochemical window for high energy solid-state lithium batteries,' *InfoMat*, vol. 5, no. 3, e12394, Mar. 2023, ISSN: 2567-3165. DOI: `10.1002/INF2.12394`.

[44] P. U. Nzereogu et al., 'Solid-State lithium-ion battery electrolytes: Revolutionizing energy density and safety,' *Hybrid Advances*, vol. 8, p. 100 339, Mar. 2025, ISSN: 2773-207X. DOI: `10.1016/J.HYBADV.2024.100339`.

[45] V. Thangadurai and W. Weppner, 'Li6ALa2Ta2O12 (A=Sr,Ba): Novel Garnet-Like Oxides for Fast Lithium Ion Conduction,' *Advanced Functional Materials*, vol. 15, no. 1, pp. 107–112, Jan. 2005, ISSN: 1616-3028. DOI: `10.1002/ADFM.200400044`.

[46] R. Murugan, V. Thangadurai and W. Weppner, 'Fast lithium ion conduction in garnet-type Li7La 3Zr2O12,' *Angewandte Chemie - International Edition*, vol. 46, no. 41, pp. 7778–7781, 2007, ISSN: 14337851. DOI: `10.1002/ANIE.200701144`.

[47] S. Yu et al., 'Elastic Properties of the Solid Electrolyte Li7La3Zr2O12 (LLZO),' *Chemistry of Materials*, vol. 28, no. 1, pp. 197–206, Jan. 2016, ISSN: 15205002. DOI: `10.1021/ACS.CHEMMATER.5B03854/ASSET/IMAGES/LARGE/CM-2015-03854A{\_}0003.JPEG`.

[48] H. Wu, H. Han, Z. Yan, Q. Zhao and J. Chen, 'Chloride solid-state electrolytes for all-solid-state lithium batteries,' *Journal of Solid State Electrochemistry*, vol. 26, no. 9, pp. 1791–1808, Sep. 2022, ISSN: 14330768. DOI: `10.1007/S10008-022-05230-X/FIGURES/3`.

[49] X. Li et al., 'Progress and perspectives on halide lithium conductors for all-solid-state lithium batteries,' *Energy & Environmental Science*, vol. 13, no. 5, pp. 1429–1461, May 2020, ISSN: 1754-5706. DOI: `10.1039/C9EE03828K`.

[50] T. Asano et al., 'Solid Halide Electrolytes with High Lithium-Ion Conductivity for Application in 4 V Class Bulk-Type All-Solid-State Batteries,' *Advanced Materials*, vol. 30, no. 44, p. 1 803 075, Nov. 2018, ISSN: 1521-4095. DOI: `10.1002/ADMA.201803075`.

[51] Y. Fu and C. Ma, 'Interplay between Li3YX6 (X = Cl or Br) solid electrolytes and the Li metal anode,' *Science China Materials*, vol. 64, no. 6, pp. 1378–1385, Jun. 2021, ISSN: 21994501. DOI: `10.1007/S40843-020-1580-3/METRICS`.

[52] J. Lau et al., 'Sulfide Solid Electrolytes for Lithium Battery Applications,' *Advanced Energy Materials*, vol. 8, no. 27, p. 1 800 933, Sep. 2018, ISSN: 1614-6840. DOI: `10.1002/AENM.201800933`.

[53] B. Man et al., 'A Comprehensive Review of Sulfide Solid-State Electrolytes: Properties, Synthesis, Applications, and Challenges,' *Crystals 2025, Vol. 15, Page 492*, vol. 15, no. 6, p. 492, May 2025, ISSN: 2073-4352. DOI: `10.3390/CRYST15060492`.

[54] Q. Zhang, D. Cao, Y. Ma, A. Natan, P. Aurora and H. Zhu, ‘Sulfide-Based Solid-State Electrolytes: Synthesis, Stability, and Potential for All-Solid-State Batteries,’ *Advanced Materials*, vol. 31, no. 44, p. 1 901 131, Nov. 2019, ISSN: 1521-4095. DOI: `10.1002/ADMA.201901131`.

[55] S. Wenzel, T. Leichtweiss, D. Krüger, J. Sann and J. Janek, ‘Interphase formation on lithium solid electrolytes—An in situ approach to study interfacial reactions by photoelectron spectroscopy,’ *Solid State Ionics*, vol. 278, pp. 98–105, Oct. 2015, ISSN: 0167-2738. DOI: `10.1016/J.SSI.2015.06.001`.

[56] S. Wenzel, D. A. Weber, T. Leichtweiss, M. R. Busche, J. Sann and J. Janek, ‘Interphase formation and degradation of charge transfer kinetics between a lithium metal anode and highly crystalline Li7P3S11 solid electrolyte,’ *Solid State Ionics*, vol. 286, pp. 24–33, Mar. 2016, ISSN: 0167-2738. DOI: `10.1016/J.SSI.2015.11.034`.

[57] S. Wenzel et al., ‘Direct Observation of the Interfacial Instability of the Fast Ionic Conductor Li10GeP2S12 at the Lithium Metal Anode,’ *Chemistry of Materials*, vol. 28, no. 7, pp. 2400–2407, Apr. 2016, ISSN: 15205002. DOI: `10.1021/ACS.CHEMMATER.6B00610/ASSET/IMAGES/LARGE/CM-2016-00610Y{\_}0005.JPEG`.

[58] J. Maier, *Physical Chemistry of Ionic Materials: Ions and Electrons in Solids*. John Wiley & Sons, 2004.

[59] J. Janek and W. G. Zeier, ‘Challenges in speeding up solid-state battery development,’ *Nature Energy 2023 8:3*, vol. 8, no. 3, pp. 230–240, Feb. 2023, ISSN: 2058-7546. DOI: `10.1038/s41560-023-01208-9`.

[60] C. D. Alt et al., ‘Quantifying multiphase SEI growth in sulfide solid electrolytes,’ *Joule*, vol. 8, no. 10, pp. 2755–2776, Oct. 2024, ISSN: 25424351. DOI: `10.1016/J.JOULE.2024.07.006/ATTACHMENT/C0797F71-01AA-4882-B466-283E4296A5CD/MMC3.ZIP`.

[61] D. H. Tan et al., ‘Elucidating Reversible Electrochemical Redox of Li6PS5Cl Solid Electrolyte,’ *ACS Energy Letters*, pp. 2418–2427, Aug. 2019, ISSN: 23808195. DOI: `10.1021/acsenergylett.9b01693`.

[62] B. Aktekin et al., ‘Operando Photoelectron Spectroscopy Analysis of Li6PS5Cl Electrochemical Decomposition Reactions in Solid-State Batteries,’ *ACS Energy Letters*, vol. 9, no. 7, pp. 3492–3500, Apr. 2024, ISSN: 23808195. DOI: `10.1021/ACSENERGYLETT.4C01072/ASSET/IMAGES/LARGE/NZ4C01072{\_}0004.JPEG`.

[63] H. Huo and J. Janek, ‘Silicon as Emerging Anode in Solid-State Batteries,’ *ACS Energy Letters*, vol. 7, no. 11, pp. 4005–4016, Nov. 2022, ISSN: 23808195. DOI: `10.1021/ACSENERGYLETT.2C01950/ASSET/IMAGES/LARGE/NZ2C01950{\_}0005.JPEG`.

[64] C. Heubner et al., ‘From Lithium-Metal toward Anode-Free Solid-State Batteries: Current Developments, Issues, and Challenges,’ *Advanced Functional Materials*, vol. 31, no. 51, p. 2 106 608, Dec. 2021, ISSN: 1616-3028. DOI: `10.1002/ADFM.202106608`.

[65] C. Liu et al., 'Recent advances of non-lithium metal anode materials for solid-state lithium-ion batteries,' *Journal of Materials Chemistry A*, vol. 10, no. 32, pp. 16 761–16 778, Aug. 2022, ISSN: 2050-7496. DOI: `10.1039/D2TA03905B`.

[66] S. Schweidler, L. De Biasi, A. Schiele, P. Hartmann, T. Brezesinski and J. Janek, 'Volume Changes of Graphite Anodes Revisited: A Combined Operando X-ray Diffraction and in Situ Pressure Analysis Study,' *Journal of Physical Chemistry C*, vol. 122, no. 16, pp. 8829–8835, Apr. 2018, ISSN: 19327455. DOI: `10.1021/ACS.JPCC.8B01873/ASSET/IMAGES/LARGE/JP-2018-01873N{\_}0006.JPEG`.

[67] S. E. Sandoval et al., 'Electro-chemo-mechanics of anode-free solid-state batteries,' *Nature Materials 2025 24:5*, vol. 24, no. 5, pp. 673–681, Jan. 2025, ISSN: 1476-4660. DOI: `10.1038/s41563-024-02055-z`.

[68] S. H. Park, D. Jun, G. H. Lee, S. G. Lee and Y. J. Lee, 'Toward high-performance anodeless batteries based on controlled lithium metal deposition: a review,' *Journal of Materials Chemistry A*, vol. 9, no. 26, pp. 14 656–14 681, Jul. 2021, ISSN: 2050-7496. DOI: `10.1039/D1TA02657G`.

[69] C. Martin, M. Genovese, A. J. Louli, R. Weber and J. R. Dahn, 'Cycling Lithium Metal on Graphite to Form Hybrid Lithium-Ion/Lithium Metal Cells,' *Joule*, vol. 4, no. 6, pp. 1296–1310, Jun. 2020, ISSN: 2542-4351. DOI: `10.1016/J.JOULE.2020.04.003`.

[70] A. Müller et al., 'Influence of Au, Pt, and C Seed Layers on Lithium Nucleation Dynamics for Anode-Free Solid-State Batteries,' *ACS Applied Materials and Interfaces*, vol. 16, no. 1, pp. 695–703, Jan. 2024, ISSN: 19448252. DOI: `10.1021/ACSAMI.3C14693/ASSET/IMAGES/LARGE/AM3C14693{\_}0005.JPEG`.

[71] J. S. Kim et al., 'Surface engineering of inorganic solid-state electrolytes via interlayers strategy for developing long-cycling quasi-all-solid-state lithium batteries,' *Nature Communications 2023 14:1*, vol. 14, no. 1, pp. 782–, Feb. 2023, ISSN: 2041-1723. DOI: `10.1038/s41467-023-36401-7`.

[72] Y. G. Lee et al., 'High-energy long-cycling all-solid-state lithium metal batteries enabled by silver–carbon composite anodes,' *Nature Energy*, vol. 5, no. 4, pp. 299–308, Apr. 2020, ISSN: 20587546. DOI: `10.1038/s41560-020-0575-z`.

[73] S. E. Sandoval et al., 'Structural and electrochemical evolution of alloy interfacial layers in anode-free solid-state batteries,' *Joule*, vol. 7, no. 9, pp. 2054–2073, Sep. 2023, ISSN: 2542-4351. DOI: `10.1016/J.JOULE.2023.07.022`.

[74] K. B. Hatzell, 'Anode-Less or Anode-Free?' *ACS Energy Letters*, vol. 8, no. 11, pp. 4775–4776, Nov. 2023, ISSN: 23808195. DOI: `10.1021/ACSENERGYLETT.3C02163/ASSET/IMAGES/LARGE/NZ3C02163{\_}0001.JPEG`.

[75] B. J. Neudecker, N. J. Dudney and J. B. Bates, '"Lithium-Free" Thin-Film Battery with In Situ Plated Li Anode,' *Journal of The Electrochemical Society*, vol. 147, no. 2, p. 517, Feb. 2000, ISSN: 00134651. DOI: `10.1149/1.1393226/XML`.

[76] S. K. Otto et al., 'Storage of Lithium Metal: The Role of the Native Passivation Layer for the Anode Interface Resistance in Solid State Batteries,' *ACS Applied Energy Materials*, vol. 4, no. 11, pp. 12 798–12 807, Nov. 2021, ISSN: 25740962. DOI: `10.1021/ACSAEM.1C02481/ASSET/IMAGES/LARGE/AE1C02481{\_}0007.JPEG`.

[77] J. Rizell, W. Chrobak, N. Mozhzhukhina, S. Xiong and A. Matic, 'Electrochemical Signatures of Potassium Plating and Stripping,' *Journal of The Electrochemical Society*, vol. 171, no. 2, p. 020 517, Feb. 2024, ISSN: 1945-7111. DOI: `10.1149/1945-7111/AD2593`.

[78] M. Sadd, S. Xiong, J. R. Bowen, F. Marone and A. Matic, 'Investigating microstructure evolution of lithium metal during plating and stripping via operando X-ray tomographic microscopy,' *Nature Communications 2023 14:1*, vol. 14, no. 1, pp. 854–, Feb. 2023, ISSN: 2041-1723. DOI: `10.1038/s41467-023-36568-z`.

[79] Q. Wang et al., 'Clarifying the Relationship between the Lithium Deposition Coverage and Microstructure in Lithium Metal Batteries,' *Journal of the American Chemical Society*, vol. 144, no. 48, pp. 21 961–21 971, Dec. 2022, ISSN: 15205126. DOI: `10.1021/JACS.2C08849/ASSET/IMAGES/LARGE/JA2C08849{\_}0008.JPEG`.

[80] M. J. Wang, E. Carmona, A. Gupta, P. Albertus and J. Sakamoto, 'Enabling "lithium-free" manufacturing of pure lithium metal solid-state batteries through in situ plating,' en, *Nature Communications*, vol. 11, no. 1, p. 5201, Oct. 2020, ISSN: 2041-1723. DOI: `10.1038/s41467-020-19004-4`.

[81] J. Janek et al., *Imaging the Microstructure of Lithium and Sodium Metal in "Anode-Free" Solid-State Batteries using EBSD*, en, May 2024. DOI: `10.21203/rs.3.rs-4466249/v1`.

[82] Z. Ning et al., 'Dendrite initiation and propagation in lithium metal solid-state batteries,' *Nature*, vol. 618, no. 7964, pp. 287–293, Jun. 2023, ISSN: 14764687. DOI: `10.1038/s41586-023-05970-4`.

[83] Y. Ren, Y. Shen, Y. Lin and C.-W. Nan, 'Direct observation of lithium dendrites inside garnet-type lithium-ion solid electrolyte,' *Electrochemistry Communications*, vol. 57, pp. 27–30, Aug. 2015, ISSN: 1388-2481. DOI: `10.1016/j.elecom.2015.05.001`.

[84] Y. Song et al., 'Revealing the Short-Circuiting Mechanism of Garnet-Based Solid-State Electrolyte,' *Advanced Energy Materials*, vol. 9, no. 21, p. 1 900 671, Jun. 2019, ISSN: 1614-6840. DOI: `10.1002/AENM.201900671`.

[85] F. Aguesse et al., 'Investigating the dendritic growth during full cell cycling of garnet electrolyte in direct contact with Li metal,' *ACS Applied Materials and Interfaces*, vol. 9, no. 4, pp. 3808–3816, Feb. 2017, ISSN: 19448252. DOI: `10.1021/ACSAMI.6B13925/ASSET/IMAGES/LARGE/AM-2016-13925C{\_}0006.JPEG`.

[86] T. Cao et al., 'Chemomechanical Origins of the Dynamic Evolution of Isolated Li Filaments in Inorganic Solid-State Electrolytes,' *Nano Letters*, vol. 24, no. 6, pp. 1843–1850, Feb. 2024, ISSN: 15306992. DOI: `10.1021/ACS.NANOLETT.3C03321/SUPPL{\_}FILE/NL3C03321{\_}SI{\_}003.MP4`.

[87] W. S. LePage et al., 'Lithium Mechanics: Roles of Strain Rate and Temperature and Implications for Lithium Metal Batteries,' *Journal of The Electrochemical Society*, vol. 166, no. 2, A89–A97, Jan. 2019, ISSN: 0013-4651. DOI: `10.1149/2.0221902JES/DATA`.

[88] L. Porz et al., 'Mechanism of Lithium Metal Penetration through Inorganic Solid Electrolytes,' *Advanced Energy Materials*, vol. 7, no. 20, p. 1 701 003, Oct. 2017, ISSN: 1614-6840. DOI: `10.1002/AENM.201701003`.

[89] H. Schmalzried and J. Janek, 'Chemical kinetics of phase boundaries in solids,' *Berichte der Bunsengesellschaft/Physical Chemistry Chemical Physics*, vol. 102, no. 2, pp. 127–143, 1998, ISSN: 0940483X. DOI: `10.1002/BBPC.19981020202`.

[90] T. Krauskopf, H. Hartmann, W. G. Zeier and J. Janek, 'Toward a Fundamental Understanding of the Lithium Metal Anode in Solid-State Batteries - An Electrochemo-Mechanical Study on the Garnet-Type Solid Electrolyte Li 6.25 Al 0.25 La 3 Zr 2 O 12,' *ACS Applied Materials and Interfaces*, vol. 11, no. 15, pp. 14 463–14 477, Apr. 2019, ISSN: 19448252. DOI: `10.1021/ACSAMI.9B02537/ASSET/IMAGES/LARGE/AM-2019-02537N{\_}0003.JPEG`.

[91] J. K. Eckhardt, P. J. Klar, J. Janek and C. Heiliger, 'Interplay of Dynamic Constriction and Interface Morphology between Reversible Metal Anode and Solid Electrolyte in Solid State Batteries,' *ACS Applied Materials and Interfaces*, vol. 14, no. 31, pp. 35 545–35 554, Aug. 2022, ISSN: 19448252. DOI: `10.1021/ACSAMI.2C07077/ASSET/IMAGES/LARGE/AM2C07077{\_}0008.JPEG`.

[92] J. Kasemchainan et al., 'Critical stripping current leads to dendrite formation on plating in lithium anode solid electrolyte cells,' *Nature Materials*, vol. 18, no. 10, pp. 1105–1111, Oct. 2019, ISSN: 14764660. DOI: `10.1038/s41563-019-0438-9`.

[93] P. Barai, T. Fuchs, E. Trevisanello, F. H. Richter, J. Janek and V. Srinivasan, 'Study of Void Formation at the Lithium—Solid Electrolyte Interface,' *Chemistry of Materials*, vol. 36, no. 5, pp. 2245–2258, Mar. 2024, ISSN: 15205002. DOI: `10.1021/ACS.CHEMMATER.3C01708/ASSET/IMAGES/LARGE/CM3C01708{\_}0010.JPEG`.

[94] S. Lang et al., 'Formation, Growth, and Shrinkage of Voids in Lithium Metal in Contact With an LLZO Electrolyte,' *ACS Applied Materials and Interfaces*, vol. 17, no. 41, pp. 56 980–56 990, Oct. 2025, ISSN: 19448252. DOI: `10.1021/ACSAMI.5C09594/ASSET/IMAGES/LARGE/AM5C09594{\_}0010.JPEG`.

[95] M. J. Wang, R. Choudhury and J. Sakamoto, 'Characterizing the Li-Solid-Electrolyte Interface Dynamics as a Function of Stack Pressure and Current Density,' *Joule*, vol. 3, no. 9, pp. 2165–2178, Sep. 2019, ISSN: 2542-4351. DOI: `10.1016/J.JOULE.2019.06.017`.

[96] *Void growth in the lithium anode of a solid state battery - ScienceDirect.*

[97] P. Peljo and H. H. Girault, 'Electrochemical potential window of battery electrolytes: the HOMO–LUMO misconception,' *Energy & Environmental Science*, vol. 11, no. 9, pp. 2306–2309, Sep. 2018, ISSN: 1754-5706. DOI: `10.1039/C8EE01286E`.

[98] B. Aktekin, L. M. Riegger, S. K. Otto, T. Fuchs, A. Henss and J. Janek, 'SEI growth on Lithium metal anodes in solid-state batteries quantified with coulometric titration time analysis,' *Nature Communications 2023 14:1*, vol. 14, no. 1, pp. 6946–, Oct. 2023, ISSN: 2041-1723. DOI: `10.1038/s41467-023-42512-y`.

[99] M. Burton et al., 'The role of phosphorus in the solid electrolyte interphase of argyrodite solid electrolytes,' *Nature Communications 2025 16:1*, vol. 16, no. 1, pp. 9304–, Oct. 2025, ISSN: 2041-1723. DOI: `10.1038/s41467-025-64357-3`.

[100] S. Narayanan, U. Ulissi, J. S. Gibson, Y. A. Chart, R. S. Weatherup and M. Pasta, 'Effect of current density on the solid electrolyte interphase formation at the lithiumLi6PS5Cl interface,' *Nature Communications 2022 13:1*, vol. 13, no. 1, pp. 7237–, Nov. 2022, ISSN: 2041-1723. DOI: `10.1038/s41467-022-34855-9`.

[101] S. K. Otto et al., 'In Situ Investigation of Lithium Metal–Solid Electrolyte Anode Interfaces with ToF-SIMS,' *Advanced Materials Interfaces*, vol. 9, no. 13, p. 2 102 387, May 2022, ISSN: 2196-7350. DOI: `10.1002/ADMI.202102387`.

[102] V. I. Yamakov et al., 'Pressure Dependence of Solid Electrolyte Ionic Conductivity: A Particle Dynamics Study,' *ACS Applied Materials and Interfaces*, vol. 15, no. 22, pp. 27 243–27 252, Jun. 2023, ISSN: 19448252. DOI: `10.1021/ACSAMI.3C01279/ASSET/IMAGES/LARGE/AM3C01279{\_}0008.JPEG`.

[103] S. Puls et al., 'Benchmarking the reproducibility of all-solid-state battery cell performance,' *Nature Energy 2024 9:10*, vol. 9, no. 10, pp. 1310–1320, Sep. 2024, ISSN: 2058-7546. DOI: `10.1038/s41560-024-01634-3`.

[104] J. Zhang et al., 'Challenges and Strategies of Low-Pressure All-Solid-State Batteries,' *Advanced Materials*, vol. 37, no. 6, p. 2 413 499, Apr. 2025, ISSN: 1521-4095. DOI: `10.1002/ADMA.202413499`.

[105] J. M. Doux et al., 'Stack Pressure Considerations for Room-Temperature All-Solid-State Lithium Metal Batteries,' *Advanced Energy Materials*, vol. 10, no. 1, p. 1 903 253, Jan. 2020, ISSN: 1614-6840. DOI: `10.1002/AENM.201903253`.

[106] C. Lee et al., 'Stack Pressure Measurements to Probe the Evolution of the Lithium-Solid-State Electrolyte Interface,' *ACS Energy Letters*, vol. 6, no. 9, pp. 3261–3269, Sep. 2021, ISSN: 23808195. DOI: `10.1021/ACSENERGYLETT.1C01395/ASSET/IMAGES/LARGE/NZ1C01395{\_}0005.JPEG`.

[107] J. Sivavec, K. V. Kravchyk and M. V. Kovalenko, 'Impact of stack pressure on coulometric titration time analysis,' *Communications Chemistry 2025 8:1*, vol. 8, no. 1, pp. 96–, Apr. 2025, ISSN: 2399-3669. DOI: `10.1038/s42004-025-01496-0`.

[108] J. Maibach, J. Rizell, A. Matic and N. Mozhzhukhina, 'Toward Operando Characterization of Interphases in Batteries,' *ACS Materials Letters*, vol. 5, no. 9, pp. 2431–2444, Sep. 2023, ISSN: 26394979. DOI: `10.1021/ACSMATERIALSLETT.3C00207/ASSET/IMAGES/LARGE/TZ3C00207{\_}0005.JPEG`.

[109] J. K. Eckhardt, T. Fuchs, S. Burkhardt, P. J. Klar, J. Janek and C. Heiliger, '3D Impedance Modeling of Metal Anodes in Solid-State Batteries-Incompatibility of Pore Formation and Constriction Effect in Physical-Based 1D Circuit Models,' *ACS Applied Materials and Interfaces*, vol. 14, no. 37, pp. 42 757–42 769, Sep. 2022, ISSN: 19448252. DOI: `10.1021/ACSAMI.2C12991/ASSET/IMAGES/LARGE/AM2C12991{\_}0007.JPEG`.

[110] J. A. Lewis et al., 'Linking void and interphase evolution to electrochemistry in solid-state batteries using operando X-ray tomography,' *Nature Materials*, vol. 20, no. 4, pp. 503–510, Apr. 2021, ISSN: 14764660. DOI: `10.1038/s41563-020-00903-2`.

[111] M. B. Dixit et al., 'Synchrotron imaging of pore formation in Li metal solid-state batteries aided by machine learning,' *ACS Applied Energy Materials*, vol. 3, no. 10, pp. 9534–9542, Oct. 2020, ISSN: 25740962. DOI: `10.1021/ACSAEM.0C02053/ASSET/IMAGES/MEDIUM/AE0C02053{\_}M009.GIF`.

[112] H. Wang et al., 'Internal pressure regulation enables reliable electrochemical performance evaluation of lithium-ion full coin cell,' *Journal of Power Sources*, vol. 600, p. 234 235, Apr. 2024, ISSN: 0378-7753. DOI: `10.1016/J.JPOWSOUR.2024.234235`.

[113] *Investigating the densification of Li6PS5Cl solid electrolyte through multi-scale characterization techniques - ScienceDirect.*

[114] E. Schlautmann et al., 'Impact of the Solid Electrolyte Particle Size Distribution in Sulfide-Based Solid-State Battery Composites,' en, *Advanced Energy Materials*, vol. 13, no. 41, p. 2 302 309, Nov. 2023, ISSN: 1614-6840. DOI: `10.1002/aenm.202302309`.

[115] C. Lee et al., 'Enhancing electrochemomechanics: How stack pressure regulation affects all-solid-state batteries,' *Energy Storage Materials*, vol. 66, p. 103 196, Feb. 2024, ISSN: 2405-8297. DOI: `10.1016/J.ENSM.2024.103196`.

[116] A. J. Bard and L. R. Faulkner, *Electrochemical Methods. Fundamentals and Applications*, Second. John Wiley & Sons, INC., 2001.

[117] J. A. Lewis et al., 'Role of Areal Capacity in Determining Short Circuiting of Sulfide-Based Solid-State Batteries,' *ACS Applied Materials and Interfaces*, vol. 14, no. 3, pp. 4051–4060, Jan. 2022, ISSN: 19448252. DOI: `10.1021/ACSAMI.1C20139/ASSET/IMAGES/LARGE/AM1C20139{\_}0006.JPEG`.

[118] P. Vadhva et al., 'Electrochemical Impedance Spectroscopy for All-Solid-State Batteries: Theory, Methods and Future Outlook,' *ChemElectroChem*, vol. 8, no. 11, pp. 1930–1947, Jun. 2021, ISSN: 2196-0216. DOI: `10.1002/CELC.202100108`.

[119] J. A. Lewis et al., 'Accelerated Short Circuiting in Anode-Free Solid-State Batteries Driven by Local Lithium Depletion,' *Advanced Energy Materials*, vol. 13, no. 12, p. 2 204 186, Mar. 2023, ISSN: 1614-6840. DOI: `10.1002/AENM.202204186`.

[120] E. Barsoukov and J. R. Macdonald, *Impedance Spectroscopy : Theory, Experiment, and Applications*, 3rd ed., E. Barsoukov and J. R. Macdonald, Eds. John Wiley & Sons, Incorporated, 2018.

[121] S. Hori et al., 'Understanding the impedance spectra of all-solid-state lithium battery cells with sulfide superionic conductors,' *Journal of Power Sources*, vol. 556, p. 232 450, Feb. 2023, ISSN: 0378-7753. DOI: `10.1016/J.JPOWSOUR.2022.232450`.

[122] T. H. Wan, M. Saccoccio, C. Chen and F. Ciucci, 'Influence of the Discretization Methods on the Distribution of Relaxation Times Deconvolution: Implementing Radial Basis Functions with DRTtools,' *Electrochimica Acta*, vol. 184, pp. 483–499, Dec. 2015, ISSN: 0013-4686. DOI: `10.1016/J.ELECTACTA.2015.09.097`.

[123] Z. Wang et al., 'DRTtools: Freely Accessible Distribution of Relaxation Times Analysis for Electrochemical Impedance Spectroscopy,' *ACS Electrochemistry*, vol. 1, no. 12, pp. 2680–2689, Dec. 2025, ISSN: 2997-0571. DOI: `10.1021/ACSELECTROCHEM.5C00334`.

[124] C. Plank et al., 'A review on the distribution of relaxation times analysis: A powerful tool for process identification of electrochemical systems,' *Journal of Power Sources*, vol. 594, p. 233 845, Feb. 2024, ISSN: 0378-7753. DOI: `10.1016/J.JPOWSOUR.2023.233845`.

[125] I. Capone et al., 'Electrochemo-Mechanical Properties of Red Phosphorus Anodes in Lithium, Sodium, and Potassium Ion Batteries,' *Matter*, vol. 3, no. 6, pp. 2012–2028, Dec. 2020, ISSN: 25902385. DOI: `10.1016/J.MATT.2020.09.017/ATTACHMENT/BD9BD620-566E-4650-BA5F-4E79120DE078/MMC9.PDF`.

[126] P. Willmott, *An Introduction to Synchrotron Radiation : Techniques and Applications*, Second. John Wiley & Sons, Incorporated, 2019.

[127] P. Pietsch and V. Wood, 'X-Ray Tomography for Lithium Ion Battery Research: A Practical Guide,' *Annual Review of Materials Research*, vol. 47, no. Volume 47, 2017, pp. 451–479, Jul. 2017, ISSN: 15317331. DOI: `10.1146/ANNUREV-MATSCI-070616-123957/1`.

[128] P. Cloetens et al., 'Holotomography: Quantitative phase tomography with micrometer resolution using hard synchrotron radiation x rays,' *Applied Physics Letters*, vol. 75, no. 19, pp. 2912–2914, Nov. 1999, ISSN: 0003-6951. DOI: `10.1063/1.125225`.

[129] R. Khubbutdinov, A. P. Menushenkov and I. A. Vartanyants, 'Coherence properties of the high-energy fourth-generation X-ray synchrotron sources,' *Journal of Synchrotron Radiation*, vol. 26, no. Pt 6, pp. 1851–1862, Nov. 2019, ISSN: 16005775. DOI: `10.1107/S1600577519013079/PP5149SUP1.PDF`.

[130] V. Vanpeene et al., 'Comparative Study of the Quantitative Analysis of Battery Materials with X-ray Nano-tomography: From Ex Situ toward Operando Measurements,' *ACS Nano*, vol. 19, no. 10, pp. 9994–10 012, Mar. 2025, ISSN: 1936086X. DOI: `10.1021/ACSNANO.4C16419/ASSET/IMAGES/LARGE/NN4C16419{\_}0009.JPEG`.

[131] J. Rizell et al., 'Revealing Li growth modes using X-ray nano-tomography,' Aug. 2025. DOI: `10.26434/CHEMRXIV-2025-WF4WX-V2`.

[132] V. Vanpeene, O. Stamati, F. Cadiou, Q. Jacquet, J. Villanova and S. Lyonnard, '4D operando X-ray nano-holo-tomography reveals multiscale chemomechanics in Silicon-Graphite anode,' Aug. 2025.

[133] G. George, R. M. Oommen, S. Shelly, S. S. Philipose and A. M. Varghese, 'A Survey on Various Median Filtering Techniques For Removal of Impulse Noise From Digital Image,' *Proc. IEEE Conference on Emerging Devices and Smart Systems, ICEDSS 2018*, pp. 235–238, Nov. 2018. DOI: `10.1109/ICEDSS.2018.8544273`.

[134] S. Berg et al., 'ilastik: interactive machine learning for (bio)image analysis,' *Nature Methods 2019 16:12*, vol. 16, no. 12, pp. 1226–1232, Sep. 2019, ISSN: 1548-7105. DOI: `10.1038/s41592-019-0582-9`.

[135] J. Ahrens, B. Geveci and C. Law, 'ParaView: An End-User Tool for Large-Data Visualization,' *Visualization Handbook*, pp. 717–731, Jan. 2005. DOI: `10.1016/B978-012387582-2/50038-1`.

[136] J. Schindelin et al., 'Fiji: an open-source platform for biological-image analysis,' *Nature Methods 2012 9:7*, vol. 9, no. 7, pp. 676–682, Jun. 2012, ISSN: 1548-7105. DOI: `10.1038/nmeth.2019`.

[137] *plaid-xrd · PyPI.*

[138] B. Jagger and M. Pasta, 'Solid electrolyte interphases in lithium metal batteries,' *Joule*, vol. 7, no. 10, pp. 2228–2244, Oct. 2023, ISSN: 2542-4785. DOI: `10.1016/J.JOULE.2023.08.007`.